ULTRALOW-LOSS LITHIUM NIOBATE PHOTONIC INTEGRATED CIRCUITS FOR NONLINEAR AND ELECTRO-OPTIC APPLICATIONS

Yan Gao



CHALMERS

Photonics Laboratory
Department of Microtechnology and Nanoscience (MC2)
Chalmers University of Technology
Göteborg, Sweden, 2025

ULTRALOW-LOSS LITHIUM NIOBATE PHOTONIC INTEGRATED CIRCUITS FOR NONLINEAR AND ELECTRO-OPTIC APPLICATIONS
Yan Gao
(©) Yan Gao, 2025

ISBN 978-91-8103-242-0 Doktorsavhandlingar vid Chalmers tekniska högskola, Ny serie nr 5700 ISSN 0346-718X

Photonics Laboratory
Department of Microtechnology and Nanoscience (MC2)
Chalmers University of Technology
SE-412 96 Göteborg
Sweden
Telephone: +46 (0)31-772 10 00

Front cover illustration: The schematic illustration of a Kerr soliton comb in microring resonator, a supercontinuum comb in long spiral waveguide, and an electro-optic modulator.

Printed by Chalmers Reproservice Chalmers Tekniska Högskola Göteborg, Sweden, 2025 ULTRALOW-LOSS LITHIUM NIOBATE PHOTONIC INTEGRATED CIRCUITS FOR NONLINEAR AND ELECTRO-OPTIC APPLICATIONS

Yan Gao

Photonics Laboratory

Department of Microtechnology and Nanoscience (MC2) Chalmers University of Technology

Abstract

Lithium niobate (LN) has emerged as a promising integrated photonic platform due to its unique combination of electro-optic, nonlinear, and acousto-optic properties, combined with broad optical transparency, high refractive index contrast, and ultra-low optical losses. These characteristics enable diverse applications including high-speed modulators, frequency combs, quantum light sources, and nonlinear wavelength converters.

A critical challenge in LN photonics lies in fabricating tightly confined waveguides through dry etching of this chemically and physically stable material. Although the 2017 Harvard breakthrough demonstrated ultralow-loss waveguides using pure physical etching, most subsequent implementations employed partially etched structures with compromised light confinement due to etching selectivity limitations.

To further increase the light confinement, in this thesis, a fully etched LN waveguide with an etching depth of 600 nm was demonstrated. The fully etched waveguides showed significantly improved light confinement (4-fold improvement compared to the partially etched waveguides), while maintaining an ultralow propagation loss of 5.8 dB/m. Relying on the fully etched waveguide platform, we demonstrated a few nonlinear applications, such as high repetition rate Kerr microcombs (500 GHz), octave-spanning supercontinuum combs, and stimulated Brillouin scattering. To extend the functionalities of our LN waveguide platform, we also studied efficient high-speed modulators and sought the possibility of co-integration with nonlinear devices.

The developed platform significantly enhances the light-matter interaction while maintaining fabrication compatibility, opening new possibilities for complex photonic systems.

Keywords: lithium niobate, microcombs, supercontinuum, microresonators, low loss waveguides, electro-optic modulators, nonlinear optics

Publications

This thesis is based on the work contained in the following papers:

- [A] Y. Gao, F. Lei, M. Girardi, Z. Ye, R. Van Laer, V. Torres-Company, and J. Schröder, "Compact lithium niobate microring resonators in the ultrahigh q/v regime", Opt. Lett. 48, 3949, 2023.
- [B] Y. Gao, Y. Sun, I. Rebolledo-Salgado, R. Van Laer, V. Torres-Company, and J. Schröder, "Tightly-Confined and Long Z-Cut Lithium Niobate Waveguide with Ultralow-Loss", Laser Photonics Rev, p. e00042, 2025.
- [C] Y. Gao, V. Torres-Company, and J. Schröder, "Suppressed plasmonic mode coupling for efficient electro-optic lithium niobate modulator", Manuscript accepted by Opt. Express, 2025.
- [D] V. Talebi, M. Girardi, Y. Gao, F. N. A. Labbé, V. Torres-Company, Y. Ding, M. Pu, and K. Yvind, "Fabrication Tolerant Heterogeneously Integrated Lithium Niobate Modulator on Bi-Layer Silicon Nitride Using Micro Transfer Printing", in Conference on Lasers and Electro-Optics Europe (CLEO/Europe), CE-6.2, 2025.
- [E] L. Haerteis, Y. Gao, A. Dubey, M. K. Schmidt, P. Thurgood, G. Ren, J. Schröder, D. Marpaung, A. Mitchell, M. J. Steel, A. Boes "Suspended Z-cut lithium niobate waveguides for stimulated Brillouin scattering." submitted, under review in APL Photonics, preprint avaible: arXiv:2504.07333, 2025.

Related publications and conference contributions by the author, not included in the thesis:

- [F] F. Lei, Y. Sun, Ó. B. Helgason, Z. Ye, Y. Gao, M. Karlsson, P. A. Andrekson, and V. Torres-Company, "Self-injection-locked optical parametric oscillator based on microcombs", Optica. 11, 3, 420-426, 2024.
- [G] F. Lei, Z. Ye, K. Twayana, Y. Gao, M. Girardi, Ó. B. Helgason, P. Zhao, and V. Torres-Company, "Hyperparametric oscillation via bound states in the continuum", Phys. Rev. Lett., 130, 9, p093801, 2023.
- [H] Y. Gao, F. Lei, M. Girardi, R. Van Laer, V. Torres-Company; J. Schröder, "Low-loss compact lithium niobate photonic integrated circuits", in Conference on Lasers and Electro-Optics Europe (CLEO/Europe), CK-1.4, 2023.
 - Y. Sun, F. Lei, Y. Gao, V. Torres-Company, "High-power optical parametric oscillators in silicon nitride", in Conference on Lasers and Electro-Optics Europe (CLEO/Europe), CD-14.1, 2025.

Contents

A	bstra	ct		iii			
P	ublic	ations		v			
A	ckno	wledge	ement	ix			
A	crony	Introduction					
1	Inti	roduct	ion	1			
	1.1	Overv	riew of integrated photonics	1			
				2			
		1.1.2		3			
	1.2	Lithiu	ım niobate photonics	4			
		1.2.1	Efforts towards tightly-confined LN waveguides with				
			ultralow-loss	4			
	1.3	This t	chesis	7			
	1.4	Thesis	s outline	8			
2	Litl	nium n	niobate: material and waveguide basics	9			
	2.1	Material properties of LN					
	2.2	Optical waveguides and light confinement					
2	2.3	Waveguide Losses					
	2.4	Mode	hybridization and conversion in LN waveguides	15			
3	Fab	ricatio	on techniques for ultra-low loss lithium niobate	•			
	wav	eguide	es es				
	3.1	Overv	-				
		3.1.1					
		3.1.2	Fabrication steps for electro-optic modulators	18			

	3.2	Electron beam lithography	20		
	3.3	Ion beam etching	21		
	3.4	Challenges	23		
		3.4.1 Adhesion issues between LN and ma-N 2405	23		
		3.4.2 Heat accumulation during etching	23		
		3.4.3 Resist resistance and dose optimization	25		
		3.4.4 Others	26		
4	Third-order nonlinear applications in lithium niobate				
	4.1	Dispersion engineering	27		
	4.2	Supercontinuum generation	29		
	4.3	Kerr-comb generation in LN microresonators	31		
5	Effi	cient electro-optic modulators in lithium niobate	33		
	5.1	Electro-optic modulator	33		
	5.2	Electro-optic effect in lithium niobate	34		
	5.3	Static electro-optic response	37		
	5.4	Optical loss and plasmonic mode coupling			
	5.5	Traveling-wave modulator dynamic response	44		
		5.5.1 Mathematic description	44		
		5.5.2 Influence of RF losses	47		
		5.5.3 Influence of velocity matching	47		
		5.5.4 Influence of electrode length	49		
	5.6	Segmented electrodes	50		
6	Fut	ure outlook	53		
7	Sun	nmary of papers	55		
Pa	ners		73		

Acknowledgement

The past five years at Chalmers have been a profound journey — long, challenging, yet immensely rewarding. As I reflect on this period of intellectual growth and personal discovery, I am deeply grateful to many people who have supported, inspired, and guided me along the way.

Foremost, I owe my deepest gratitude to my supervisor, Dr. Jochen Schröder, for teaching me not only the how but also the why of scientific research. Our discussions on becoming an independent researcher were essential in shaping my academic identity. I am also incredibly grateful to my co-supervisor and examiner, Prof. Victor Torres-Company, whose sharp eye for detail and dedication to top-notch research have been a huge inspiration. My thanks also extend to my co-supervisor Prof. Raphaël Van Laer, for his probing questions and visionary insights.

I sincerely thank Prof. Fuchuan Lei, who has profound physical insight and enriched knowledge. Our stimulating discussions of phenomena, theory, and research philosophy were particularly enlightening. I also thank Dr. Zhichao Ye and Dr. Marcello Girardi, who taught me professional skills for nanofabrication. I particularly appreciate Dr. Israel Rebolledo-Salgado for his help with the free-space coupling setup. I also appreciate Dr. Krishna Sundar Twayana for the assistance with linear measurements. I thank Hans Kaimre for the help with high-speed measurement.

I gratefully acknowledge the collaboration with Dr. Andy Boes and Dr. Lisa Haerteis (University of Adelaide), and Prof. Kresten Yvind and Vahid Talebi (Technical University of Denmark).

My sincere thanks to the Chalmers cleanroom staff for maintaining our delicate equipment. I express special gratitude to Dr. Mats Hagberg for his patient guidance on ion beam etching and helping develop the etching recipe.

I thank Dr. Zonglong He and Prof. Ping Zhao for insightful discussions on system-level research directions.

Special thanks to Yi Sun, Carmen López Ortega, Sara Persia, Vijay Shekhawat, Tim Fuhrmann, and Niklas Hammerschmidt for valuable scientific exchanges.

I also thank Erik Strandberg for being my office mate; it has been a lot of fun talks, especially about Ph.D. and the mysterious academic journal.

Special thanks to my ping-pong teammates: Prof. Fuchuan Lei, Dr. Óskar B. Helgason, and Dr. Krishna Sundar Twayana. Research is hard, and ping-pong is harder.

Finally, I would like to express my sincere gratitude to my families and friends for their unconditional love and support.

Yan Gao Göteborg, Sweden July 2025

Abbreviations

BSS beam step size

CAD computer-aided design

CMOS complementary metal—oxide—semiconductor

CMP chemical mechanical polishing

CPW coplanar waveguide CRD cavity ring-down CW continuous-wave

DKS dissipative Kerr soliton EBL electro-beam lithography

EM electromagnetic EO electro-optic

FCA free carrier absorption FDTD finite-difference time-domain

FEM finite element method FWM four-wave mixing GDS graphic data system GVD group velocity dispersion

IBE ion beam etching IC integrated circuit

ICP-RIE inductively coupled plasma reactive etching

KCG Kerr comb generation

LN lithium niobate

 $LNOI \qquad lithium\mbox{-}niobate\mbox{-}on\mbox{-}insulator$

MI modulation instability

MZI Mach-Zehnder interferometer

OFDR optical frequency-domain reflectometry

PCF photonic crystal fibers

PECVD plasma enhanced chemical vapor deposition

PIC photonic integrated circuit

RF radio frequency

SCG supercontinuum generation SHG second harmonic generation

SOI silicon-on-insulator TPA two photon absorption

TW traveling wave WF writing field

Chapter 1

Introduction

The evolution of contemporary civilization relies critically on the comprehension and exploitation of electromagnetic (EM) waves. EM waves techniques mainly include wave generation, manipulation, transmission, and detection. Utilization of EM waves over large frequency ranges (radiowave, micro-wave, and optical-wave) has shaped almost all aspects of human cultural, professional, and social lives. In the 21st century, photonics, a technology of generating and harnessing photons (optical waves, with frequencies of a few hundred terahertz) for practical applications, has become indispensable in both academia and industry, where light replaces or augments electronic functions. The optical wave possesses unique advantages due to its extremely high frequency, which is several orders of magnitude larger than the microwave frequency. On the one hand, high frequency provides large bandwidth for data communication and leads to ultra-high data capacity; on the other hand, it implies an ultra-short wavelength, which significantly improves the attainable resolution in ultra-precision imaging due to the reduced diffraction limit. With the fast development of sophisticated control of optical waves, there have been notable breakthroughs in wide areas such as communication [1, 2], precision metrology [3, 4], quantum information [5, 6], bio-imaging and bio-sensing [7,8].

1.1 Overview of integrated photonics

The first transistor was successfully demonstrated in 1947, at Bell Laboratories, and the 1956 Nobel Prize in Physics was awarded jointly to J. Bardeen, W. Brattain, and W. Shockley for their research on semi-

conductors and their discovery of the transistor effect. In the 1960s, the emergence of the integrated circuit (IC) with different functional transistors revolutionized electronics, enabling the miniaturization of computers and electronic circuits. The material of choice was silicon, which is widely found in nature at very low cost. Another key advantage of silicon is that high-quality silicon dioxide insulator films can be grown thermally on the silicon surface to protect the underlying transistors. Similarly to its twin brother ICs, the concept of photonic integrated circuits (PICs), a key element of integrated photonics, was also proposed by S. E. Miller [9] in the 1960s. Usually, a photonic system relies on several discrete optical components with various functions. For example, these components include optical sources (generate light), modulators (encode electric signals onto optical carriers), low-loss interconnect waveguides (transmit light), optical amplifiers (amplify optical signals), and photodetectors (detect and receive light). These optical devices usually require a variety of different materials and fabrication techniques making it challenging to realize all of them on a single material platform (in contrast to ICs where all electronic devices can be integrated on a single silicon chip). Therefore, integrated photonics underwent a much slower development pace than integrated electronics, especially in integration density.

1.1.1 Silicon photonics

Monolithic integration of all necessary optical devices has been considered a big challenge in most materials except InP. Because of the special material properties of InP with a direct bandgap and large electro-optic (EO) coefficient, high-performance lasers/photodetectors and high-speed EO modulators can be accessible simultaneously in a single material platform. However, this "perfect" platform is not widely adopted for PICs mainly due to its high cost and low yield [10].

Silicon's unparalleled success in ICs has naturally extended to PICs, where it has emerged as a dominant platform. Silicon photonics have advantages including ultralow cost, high-volume production, exceptional yield, and reproducibility, which are unmatched by most other photonic materials. The foundation of silicon photonics lies in the silicon-oninsulator (SOI) platform, a standardized multilayer structure that enables high-performance optical waveguides. Here, light is tightly confined in a silicon core ($n = 3.48 \ @1550 \ nm$) surrounded by a SiO2 cladding ($n = 1.45 \ @1550 \ nm$). The high refractive index contrast permits submicrometer waveguide dimensions, enabling ultracompact photonic cir-

cuits. Moreover, silicon's optical transparency in the near-infrared (1.1-3.8 μ m) aligns perfectly with telecommunication bands and infrared sensing applications. Eventhough silicon lacks EO effects, high-speed modulators have been demonstrated via the plasma dispersion effect [11]. By electrically tuning free-carrier concentrations through injection, accumulation, or depletion, the refractive index of silicon can be dynamically modulated. Another unique strength of silicon photonics is that they share the same material platform with silicon ICs, theoretically allowing direct co-integration of photonic and electronic elements. This synergy paves the way for advanced optoelectronic convergence.

Despite being the leading platform for PICs, silicon photonics faces inherent material limitations that hinder its progress. A major challenge is the inability to efficiently generate light due to the indirect bandgap of silicon. Furthermore, while the high refractive index contrast enables compact waveguides, it also introduces a relatively large scattering loss (~1 dB/cm) [12]. Additionally, the existence of significant two-photon absorption (TPA) and free carrier absorption (FCA) in silicon restricts high-power applications. The above shortcomings need to be solved by other photonic materials.

1.1.2 Multi-material photonic integration

Thanks to the progress of material science, besides Si, there are other photonic materials developed that are complementary or enhanced in characteristics and performance to silicon photonics. For example, III-V compounds (such as InP, GaAs) can provide gain materials and solve the problem that silicon cannot lase; Si_3N_4 features much lower linear loss (<0.1 dB/m) and is a nearly perfect platform for third-order nonlinearities; Ferroelectric materials (LiNbO₃, LiTaO₃) can provide unique second-order nonlinearities, EO effect, piezoelectricity, etc.

Research and industry pushed to integrate different materials into a photonic platform to expand the functionalities for silicon photonics. There are mainly three different ways to achieve multi-materials integration: hybrid integration, heterogeneous integration, and monolithic heteroepitaxy. Hybrid integration is a simple way to combine multiple platforms through direct coupling [13–15]. Similarly to chip/fiber coupling, the hybrid waveguides feature a large loss at each interface (\sim a few dB). Heterogeneous integration combines multiple materials by wafer/chip bonding or micro-transfer printing [16,17], the device can be connected via 3-D inverse tapers which are aligned through lithography

techniques with high accuracy, and the interlayer loss can be smaller than 1 dB [18]. Monolithic heteroepitaxy aims to grow III-V compounds directly on silicon or other popular photonic platforms [19]. Due to lattice mismatch and the difference in thermal expansion coefficient, the defect density for epitaxial layers is much higher than that of the bulk III-V material. These defects degrade material quality and ultimately limit device performance.

1.2 Lithium niobate photonics

In recent decades, more and more material platforms have been investigated, including InP [20], Si_3N_4 [21–24], AlGaAs [25, 26], AlN [27], SiC [28], LiNbO₃ [29–35], and LiTaO₃ [36]. These photonic materials, together with silicon, constitute today's integrated photonics family. Most of these materials play one or more unique roles in the family and cannot be simply replaced by other materials. In the photonic family, LN has been considered as one of the most unique and versatile photonic platforms owing to its rich material properties that can simultaneously provide electro-optic (EO), nonlinear, and acousto-optic effects. Moreover, it exhibits a broad optical transparency window, a relatively high refractive index contrast, and ultra-low material losses [34,37–39].

1.2.1 Efforts towards tightly-confined LN waveguides with ultralow-loss

Traditional LN waveguides

Lithium niobate (LN or LiNbO₃) was first introduced as an optical material in the 1960s, coinciding with the emergence of ICs and PICs. This timeline followed the successful development of high-quality single-crystal LN using the Czochralski growth technique [40,41]. Early demonstrations with bulk LN crystals include EO modulation [42] and second harmonic generation (SHG) [43]. In the 1970s-1980s, weekly-confined waveguides were demonstrated by slightly increasing the refractive index of the material through Ti-diffusion [44] or proton exchange [45] to create the waveguide core region. Devices based on weekly confined waveguides usually have weak mode confinement, large footprint, and reduced nonlinear interactions.

Hybrid LN waveguides

Similarly to SOI, LN on insulator (LNOI) wafers have become commercially available through the development of "smart cut" technol-

Taking advantage of the LNOI platform, high confinement integrated waveguide can be achieved. There are usually two types of highly confined waveguide: hybrid waveguides and etched waveguides. LN presents significant fabrication challenges as a result of its notoriously difficult etching characteristics. To avoid this limitation, hybrid waveguides that combine LN with more easily patterned materials were used, where the waveguide is constructed by LN and another material. In a typical implementation, a secondary material with favorable etching properties (such as Si or Si₃N₄) is first deposited onto thin film LN by sputtering or plasma-enhanced chemical vapor deposition (PECVD). Then, this auxiliary layer is patterned using standard etching techniques to form the waveguide structure [47, 48]. An alternative approach for the fabrication of hybrid LN waveguides involves the bonding of LN thin films to prepatterned Si or Si₃N₄ waveguides. This heterogeneous integration strategy offers a promising route for the incorporation of LN photonics with other existing PICs [16,49,50]. Both direct material loading and heterogeneous integration methods have achieved propagation losses lower than 0.3 dB/cm. The major drawback of hybrid waveguides is that part of the optical mode is located in other material instead of LN, which results in weaker EO or nonlinear interactions.

Different types of etched LN waveguides

People have been trying to etch LN for high confinement optical waveguides with low loss for a long time. For example, a typical process [51] uses Cr as a hard mask (defined by lithography) and femtosecond laser ablation to form waveguide structures, followed by chemical mechanical polishing (CMP). Waveguides with small sidewall roughness can be obtained and very low losses of 0.027 dB/cm have been achieved [51]. However, the CMP-based process leads to a shallow waveguide structure with a large sidewall angle, limiting the minimum bending radius. Wet etching is another choice for LN waveguides where Cr or other masks are used to protect the waveguide region and corrosive liquid is used to remove the exposed LN. In the early research, a solution of 40% HF and 100% HNO₃ is used, a propagation loss of 0.3 dB/cm was achieved on LN waveguides with a top width of 6.5 µm [52]. Wet etching is also useful to improve sidewall roughness caused by residual of photo-resist mask. For example, a solution with H₂O₂, NH₄OH, and H₂O in a ratio of 2:2:1 was proven to be efficient in removing material depositions [53]. Similar solutions are now widely used for residual cleaning after dry etching of LN. Very recently, the same solution has also been used to direct wet etch LN and 10 million Q-factor resonators can be achieved in a waveguide width of 4 μ m. In general, there are a few drawbacks to wet etching, which make it less attractive. These drawbacks include: the low etching rate, and the isotropic etching, which makes it challenging to fabricate waveguides narrower than 1 μ m [37]. Like dry etching for many materials, fluorine-based reactive ion etching (RIE) is also used and can effectively remove LN [54]. However, the non-volatile byproduct LiF results in severe redeposition problems [55].

Pure physically etched LN waveguides

Currently, ion beam etching (IBE) also called ion milling [56] by Ar+ plasma is among the most popular dry etching techniques for LNOI [57]. In 2017, Harvard first demonstrated ultra-low loss (2.7 dB/m) dry etched LN waveguides at micrometer size [29]. After that, using a similar method, many other groups also achieved low loss waveguides with loss < 0.2 dB/cm [30, 58, 59]. Since there is no chemical reaction involved, pure physical bombarding will lead to a bad selectivity (usually 1:1), resulting in a shallow etched depth. Thus, most LN applications still work with partially etched waveguides with limited light confinement and a minimum bending radius of $\sim 100 \mu m$. To further enhance light confinement, in 2023, we [Paper A] demonstrated — simultaneously with EPFL [60] — the first fully etched ultralow-loss lithium niobate (LN) waveguides. These fully etched waveguides significantly improve light confinement while achieving a record-small bending radius of 20 µm, as independently demonstrated in both works. Notably, this was accomplished while maintaining ultra-low propagation losses comparable to those of partially etched waveguides.

1.2.2 Nonlinear and EO applications in LN

The ultralow-loss LN photonic platform can enable many applications in nonlinear and EO devices. By utilizing the high confined LN waveguide and the large LN's EO coefficient, COMS compatible low drive voltage and high-speed EO modulators [61,62] have been demonstrated; Owing to the large χ^2 nonlinearity and mature periodic poling technique, efficient second harmonic generation has been demonstrated [63–65]; While LN is well known as a χ^2 material, the χ^3 nonlinearity in LN is also large and the n₂ ($\sim 1.8 \times 10^{-19} \text{ m}^2/\text{W}$) in LN is comparable with the value in Si₃N₄ ($\sim 2.4 \times 10^{-19} \text{ m}^2/\text{W}$), and Kerr soliton combs in LN have also been demonstrated [30,31]. Most of the functional devices demonstrated in LNOI have been proven to be superior to their counterparts

either in bulk LN or in fibers. With the fast development of LN technology including device design and fabrication, an efficient multifunctional electro-optical on-chip system can be possible in LN PICs.

1.3 This thesis

This thesis focuses on the realization of a tightly-confined LN waveguides platform with ultralow-loss, and its applications in nonlinear and EO devices. To exploit the LN photonic platform, we started from basic waveguide fabrication and developed an LN etching method that can achieve a state-of-the-art waveguide loss down to a few dB/m. The fabrication method was first developed in [Paper A], where we achieved fully-etched waveguides and demonstrated an ultra-compact and high-Q ring resonator with a bending radius down to 20 μ m (demonstrating the highest Q/V ring resonators in LN). Then in [Paper B], we further developed our fabrication method and demonstrated the first ultralow-loss LN long waveguides (5.8 dB/m).

Based on the LN photonic platform we developed, we demonstrated a few nonlinear applications. In [Paper A], by using the compact ring resonator, we demonstrated an ultra-high repetition rate (500 GHz) soliton microcomb in LN. In [Paper B], the ultralow-loss long waveguide is used for octave-spanning supercontinuum generation, which is the first octave-spanning supercontinuum comb in the all-normal dispersion LN waveguide. Then in [Paper E], we collaborated with Adelaide University in Australia and demonstrated on chip stimulated Brillouin scattering (SBS) in a suspended thin-film lithium niobate waveguide. This work demonstrated the first SBS (other works are based on surface SBS) in TFLN waveguides.

As EO modulators are so important in LN, we further expand our work to EO devices. In [Paper C], we analyzed the optical absorption loss in lithium niobate modulators and found that the loss is dominated by mode coupling between the optical waveguide and plasmonic modes. Using this relationship, we proposed an electrode design to reduce the metal-induced absorption loss by suppressing the mode coupling. We numerically demonstrated that such a design can reduce the loss by a factor of 5 and improve the modulation efficiency by around 15%. In [Paper D], by collaborating with DTU in Demark, we demonstrated an LN-Si₃N₄ modulator by micro-transfer printing LN onto a SiN wafer. The device can utilize the advantages of the high Pockels effect in LN

and ultra-low loss in Si_3N_4 .

1.4 Thesis outline

Chapter 2 introduces the properties of LN material and the basis for LN linear waveguides. Chapter 3 introduces the fabrication techniques used in the thesis for tightly-confined ultralow-loss LN waveguides. Chapter 4 introduces third-order nonlinear applications for frequency combs in LN waveguides. Chapter 5 introduces the theory and design principles for high-speed and efficient EO modulators in LN. In the end, Chapter 6 gives a future outlook for the work in this thesis.

Chapter 2

Lithium niobate: material and waveguide basics

LN's rich material properties make it a versatile integrated photonic platform, with LN waveguides being the most important and fundamental element. For LN waveguides, one of the most important goals is to achieve higher confinement and lower loss by choosing different waveguide configurations. This chapter starts from the properties of LN materials and introduces LN waveguides, including their propagation losses and light confinement.

2.1 Material properties of LN

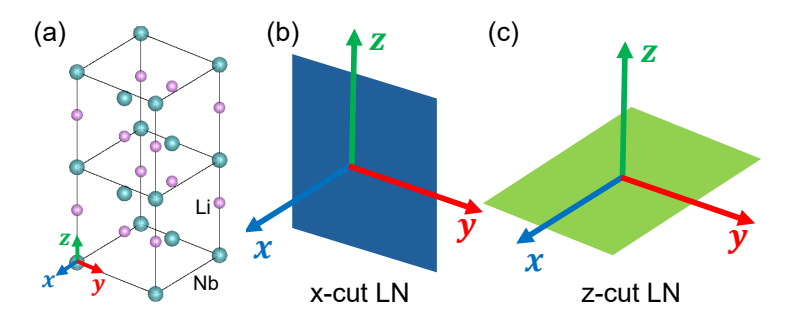


Figure 2.1: (a) Schematic diagram of the LN crystal structure, the O atoms are ignored. (b), (c) The corresponding definition of X-cut and Z-cut LN.

LN is a human synthesized ferroelectric crystal, and its crystal structure belongs to the 3m point group, which exhibits three-fold symmetry about the z-axis. Fig. 2.1(a) shows the crystal structure of LN, where the O atoms are ignored. Along the z direction, the octahedra are filled with Li, Nb, vacancy, Li, Nb, vacancy, etc. periodically. By applying a strong external electric field in the Z axis, the Li and Nb can be relocated, and Li can be moved to the adjacent vacancy, which leads to an inversion of the ferroelectric domain orientation and is used in quasiphase matching. LN has a high Curie temperature (\sim 1210 °C), which ensures a stable ferroelectric phase and is compatible with a wide range of fabrication processes and operation conditions.

Table 2.1: Summary of nonliear and EO coefficients of a few popular photonic materials. All properties are given at 1550 nm unless otherwise noted.

Material	Optical index	$\chi^2 \; (\mathrm{pm/V})$	EO coefficient (pm/V)	$n_2 \ (m^2/W)$
${ m LiNbO_3}$	2.21(o) 2.13(e)	$d_{22} = 2.1$ $d_{31} = -4.3$ $d_{33} = -27.0$ @1064 nm	$egin{array}{l} r_{13} = 9.6 \\ r_{22} = 6.8 \\ r_{33} = 30.9 \\ r_{51} = 32.6 \end{array}$	1.8×10^{-19}
Si	3.48	0	$\frac{151 - 52.0}{0}$	5×10^{-18}
SiO_2	1.44	0	0	3×10^{-20}
Si ₃ N ₄	2	0	0	2.4×10^{-19}
GaAs/ AlGaAs	3.37	$ m d_{36} = 170 \ @1064 \ nm$	$r_{41} = 1.43$	2.6×10^{-17}
AlN	2.12 (o) 2.16 (e)	$d_{31} = 1.6$ $d_{33} = 4.7$	$egin{array}{l} r_{13} = 0.67 \\ r_{33} = -0.59 \end{array}$	2.3×10^{-19}

LN is a birefringent crystal. In the normal Cartesian coordinate system, LN features ordinary refractive indices ($n_o = 2.21 \ @ 1550 \ nm$) on the x and y axes, and an extraordinary index ($n_e = 2.13 \ @ 1550 \ nm$) on the z axis. LN is transparent from 350 nm to 5000 nm, covering almost the full optical spectrum ranging from near-ultraviolet, visible, near-infrared, and mid-infrared wavelengths. In Table 2.1, we list the nonlinear and EO coefficient of LN and compare them with other popular optical materials. LN is a non-centrosymmetric crystal and features a strong second-order nonlinearity. Furthermore, owing to LN's ferroelectric domain engineering technique, reliable periodic poling and wafer scale second harmonic generation has been achieved in LN [66]. Importantly, LN is a famous EO material with a large EO coefficient ($r_{33} = 30.9 \ pm/V$). Commercial LN modulators with low loss and large bandwidth

play an important role in long-haul communication systems [67]. The third order nonlinearity in LN is also large ($n_2 = 1.8 \times 10^{-19} \,\mathrm{m}^2/\mathrm{W}$), and is comparable to other commonly used materials like $\mathrm{Si}_3\mathrm{N}_4$, which makes Kerr comb generation in LN possible. In addition to guiding photons, LN is also a suitable platform for guiding phonons, which is enabled by the fact that LN features a higher acoustic index than SiO_2 and sapphire.

2.2 Optical waveguides and light confinement

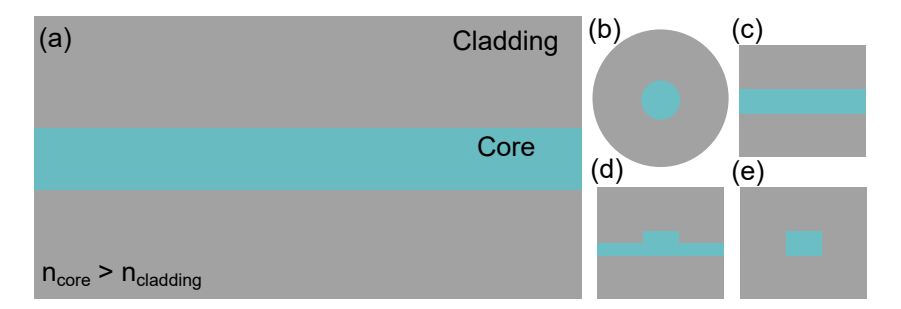


Figure 2.2: (a) Schematic diagram of optical waveguides. (b)-(e) Typical waveguides cross-sectional geometry: circular, slab, ridge, and strip optical waveguides.

The rich material properties make LN attractive for numerous photonic applications. In almost all of these applications, the most fundamental element is the optical waveguide. In the cross-sectional view, a waveguide consists of a core material with a high refractive index surrounded by one or more cladding materials with low refractive index. Along the propagation direction, the waveguide refractive index is usually uniform or equivalently uniform (such as in sub-wavelength grating waveguides [68]). A detailed discussion can be found in any textbook on guiding optics such as [69]. Figs. 2.2(b)-(e) show 4 typical waveguide structures: circular, slab, ridge, and strip waveguides, where the ridge and strip waveguides are often used in integrated optics, and circular waveguides are often used in fibers. It is noted that there are no analytic solutions for ridge or strip waveguides, and numerical simulations by computeraided design (CAD) is required in integrated photonics such as the finite element method (FEM) or the finite-difference time domain (FDTD) method.

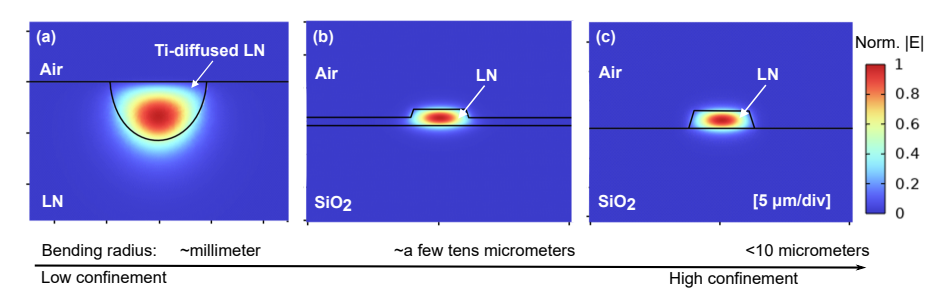


Figure 2.3: Simulated mode profiles for LN waveguides: (a) weekly-confined waveguides, (b) tightly confined partially etched waveguides, and (c) tightly confined fully etched waveguides.

There are 3 main types of LN waveguides. They are weekly confined waveguides, tightly confined partially etched waveguides, and tightly confined fully etched waveguides, as shown in Fig. 2.3. Weekly-confined waveguides are traditional LN waveguides, which are usually formed by Ti diffusion or proton exchange, where a weak refractive difference (< 0.1) is introduced to form the guiding structure. The light confinement of such waveguides is weak, having a large mode area of $\sim 100~\mu m^2$ and leading to a large bending radius of $\sim 1~mm$. The waveguide mode area is close to the mode area of a single mode fiber, which enables low interface loss (<0.5 dB). However, the weekly confined waveguide is impossible for photonic integration and dispersion engineering.

For integrated LN photonics, etching LN waveguides on the LNOI platform can form tightly confined waveguides with a mode size of micrometers and a bending radius of less than 100 µm. The tightly confined waveguides can provide two main advantages: the freedom to engineer the waveguide dispersion (by changing the waveguide geometry) and the increased light confinement. The dispersion engineering capability is a common advantage for integrated photonics which is crucial for most nonlinear applications, as will be discussed in Chapter 4. The increased light confinement can significantly enhance the nonlinear interactions, which is beneficial for efficient nonlinear processes. Moreover, high confinement waveguides can reduce the waveguide bending radius, allowing a more compact PIC. In this thesis, we focus mainly on fully etched waveguides which provide the best light confinement, and we first demonstrated high Q microring resonators with a bending radius down to 20 μ m [Paper A. We also work with partially etched waveguides for applications where optical confinement is not crucial, such as EO modulators.

2.3 Waveguide Losses

In addition to optical confinement, another crucial property of optical waveguides is the propagation loss, or attenuation factor, which is detrimental for many applications. For example, in data communications, large losses will decrease the signal-to-noise ratio (SNR) and limit the maximum transmission distance; for high-power devices, a large loss will cause significant heat problems and degrade the device performance. Therefore, reducing optical loss in waveguides is one of the most fundamental and important tasks in photonics.

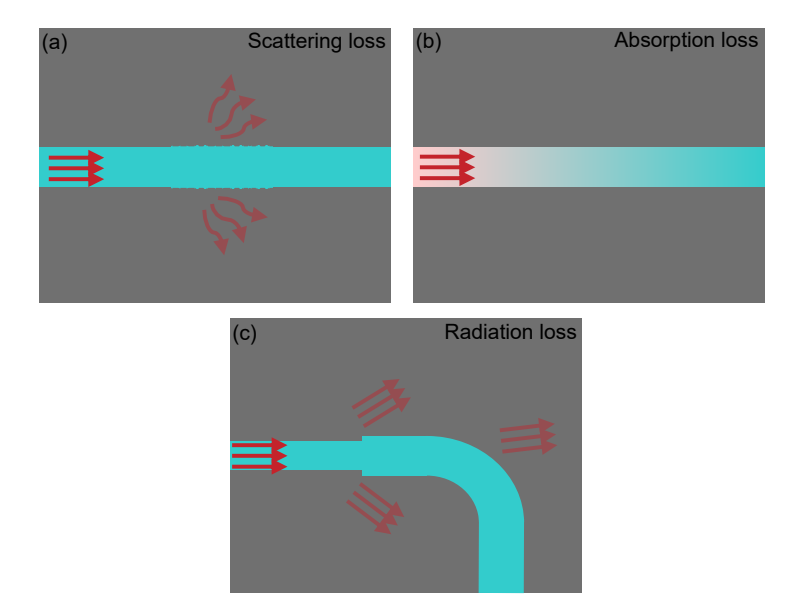


Figure 2.4: Schematic diagram of losses in optical waveguides: (a) scattering loss, (b) absorption loss, and (c) radiation loss.

Similarly to other optical waveguides, there are usually three major types of loss mechanism in LN: scattering losses, absorption losses, and radiation losses, illustrated in Fig. 2.4.

Scattering losses mainly come from the inhomogeneous refractive index of the waveguide, which will scatter light to random directions. The refractive index inhomogeneity can originate from waveguide imperfections, such as bulk, surface, or sidewall roughness. Most of the scattered light will be lost, while partial light will return back as back-scattering. In LN waveguides, the imperfect fabrication usually leads to a large sidewall roughness (~ 1 nm). This is considered the main source of scattering

losses. In the future, further optimization and new techniques such as CMP polishing or post-annealing may be introduced to reduce the side-wall roughness. The design of the waveguide geometry to reduce the light-roughness interaction strength is another solution that has been used for ultralow-loss multimode waveguides.

Absorption loss is caused by intrinsic/impurity absorption of the material, where the absorbed light energy will be transferred to heat. Using the whispering gallery resonator method, the material absorption loss in the bulk LN is measured to be <0.4 dB/m in [70] and <0.1 dB/m in [71]. Furthermore, based on [72], the material absorption Q in LNOI is as high as 163 million, which is equivalent to a loss of ~ 0.2 dB/m. This absorption loss is much smaller than the propagation loss in LN waveguides, which indicates that the propagation losses in waveguides are not limited by material absorption.

Waveguide discontinuities or waveguide bending will cause mode coupling from guided modes to radiation modes. In general, radiation losses can be minimized by proper design such as a slowly changed waveguide taper to connect two waveguides with different width. For radiation loss caused by bending, increasing the waveguide confinement and bending radius can significantly reduce it.

For integrated waveguides, there are a few different commonly used losses characterization methods, such as the microresonator method, optical frequency domain reflectometry (OFDR), and cavity ring-down (CRD) spectroscopy. The microresonator method [73] is a convenient way to measure low-loss waveguides and is used in [Paper A]. By measuring the optical spectrum of a microresonator, the optical loss can be calculated from the intrinsic Q factor of the resonator, which is extracted by using Lorentzian fitting to the optical resonances. OFDR is a high spatial resolution optical measurement that locates the loss distribution in the waveguide by analyzing the frequency domain signal of scattered light. Its core principle is based on coherent detection and frequency scanning interference [74–76]. OFDR is a non-destructive technique and can be used to detect small defects in waveguides. In [Paper B], we used OFDR to characterize the propagation loss of our long spiral waveguides. CRD is a technique that indirectly calculates the Q factor by measuring the decay time of light in an optical microresonator, based on the fact that the intensity of light in a microresonator exponentially decays over time [77, 78].

2.4 Mode hybridization and conversion in LN waveguides

The sidewall angle of Si or Si_3N_4 can be optimized to be close to 90 degrees. However, for LN waveguides, the sidewall angle is usually 60-80 degrees due to the physical etching method used for the fabrication of LN waveguides, which will be discussed in detail in Chapter 3. The non-vertical sidewall angle breaks the waveguide vertical symmetry (assuming the waveguide has top and bottom cladding with the same material) and will lead to mode coupling between the transverse electric (TE) and transverse magnetic (TM) modes. A detailed study on the influence of the sidewall angle on mode hybridization and conversion can be found in [79]. Geometric asymmetry exists also in air-cladded strip waveguides or partially etched ridge waveguides [80].

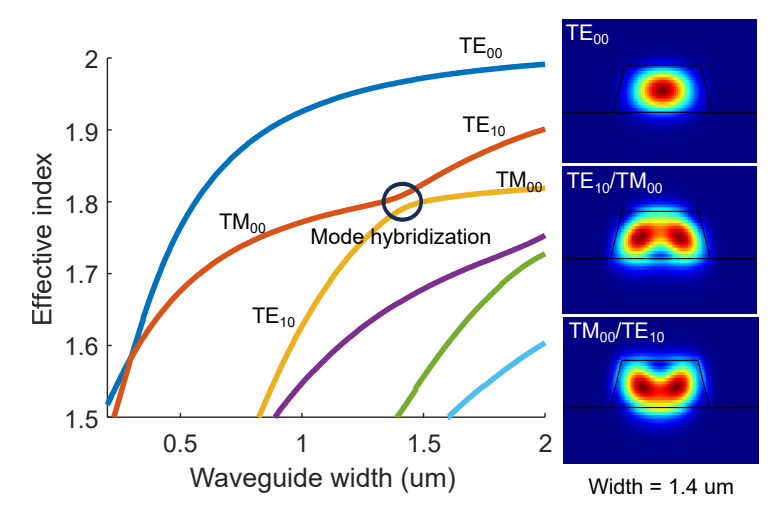


Figure 2.5: Simulated mode effective index for a typical fully etched LN waveguides and the corresponding modes for waveguide width of $1.4 \mu m$.

In Fig. 2.5, we calculated the mode effective index of a typical fully etched LN waveguide for different modes with different waveguide widths. At a waveguide width of around 1.4 μ m, hybridization of the modes between TE₁₀ and TM₀₀ occurs. Such mode hybridization will lead to a mode coupling between TM₀₀ and TE₁₀. As shown in Fig. 2.6, TM₀₀ light incident in a linear tapered LN waveguide, and almost all light is converted to the TE₁₀ mode, after a short propagation distance (a few tens of μ m). The discussed mode coupling can be useful for some

multi-mode applications such as polarization splitter-rotators. However, unwanted mode coupling will cause excess loss and crosstalk.

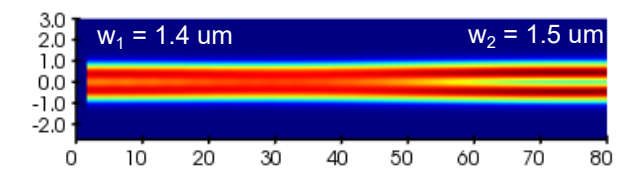


Figure 2.6: Simulated mode propagation and conversion for a linear tapered LN waveguide with an initial width of 1.4 μ m and a final width of 1.5 μ m.

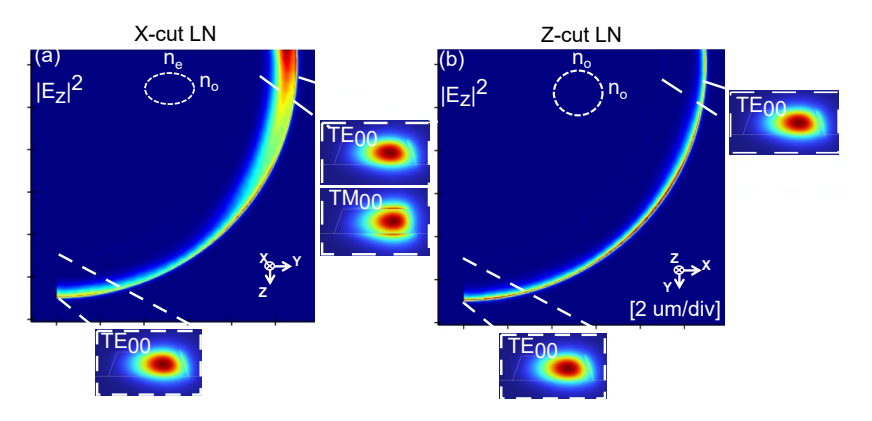


Figure 2.7: Simulated mode propagation and conversion for a linear taper LN waveguides with an initial width of 1.4 μm and a final width of 1.5 μm .

Due to the index anisotropy in LN, the undesired mode coupling can exist in an X-cut bent LN waveguide (TE mode). For an X-cut LN bent waveguide with TE mode excitation, the mode effective index will change over a different direction. The changed refractive index can cause mode coupling with other modes. Due to the lack of vertical symmetry, the coupling here includes mode coupling between the TE_{00} and TM_{00} modes, as shown in Fig. 2.7(a). Mode coupling is not seen for the case of the Z-cut LN waveguide, as shown in Fig. 2.7(b), since the refractive index in the waveguide plane is isotropic. Here we have a conclusion that for linear optics, a Z-cut LN is a better platform for the isotropic index.

Chapter 3

Fabrication techniques for ultra-low loss lithium niobate waveguides

As described in Chapter 2, thin-film LN provides a versatile optical platform for photonic applications due to its rich material properties. However, it was a long-standing challenge to achieve high confinement LN waveguides, especially with ultralow loss. In this chapter, we give an overview of the fabrication process of our LN waveguides and discuss challenges and corresponding solutions for achieving dry-etched LN waveguides with ultralow loss.

3.1 Overview of the fabrication process

3.1.1 Ultralow-loss LN waveguide fabrication

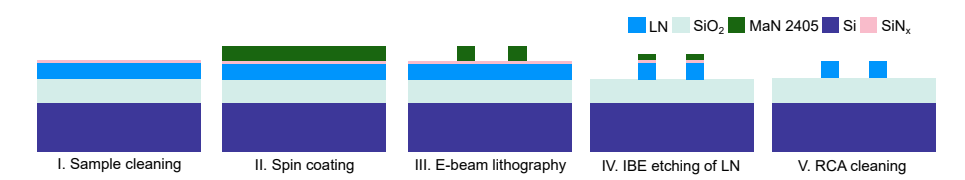


Figure 3.1: Schematic diagram of fabrication flow for ultralow-loss LN waveguides.

The ultralow-loss waveguide is one of the most important building

blocks in LN PICs, and the fabrication steps need to be carefully optimized to achieve it.

Fig. 3.1 shows the fabrication flow. LN samples are diced from a 4 inch commercial LN wafer (NANOLN). The wafer includes a thin LN film of a few hundred nanometers thickness at the top, a 525 μ m thick silicon substrate at the bottom and 4.7 μ m thermally oxidized SiO₂ in between. The sample is first prepared by solvent cleaning (acetone, IPA) and then by standard cleaning (SC1, 29% NH₃ : 30% H₂O₂ : H₂O = 1:1:5). To minimize the effect of the SC1 solution on the LN, we limit the SC1 time to 2 minutes only. The cleaned sample is then deposited with around 5 nm Si₃N₄ via vacuum sputtering (FHR, MS150), to promote adhesion between the LN and the resist. A detailed discussion can be found in Section 3.4.1.

Negative tone electro-beam lithography (EBL) resist ma-N 2405 is adopted for LN dry etching because of its high resolution, dry etch resistance, and more importantly, good thermal stability. The pattern is first defined on the resist via 100-kV EBL (Raith, EBPG 5200), in which multipass exposure is used to reduce sidewall roughness. The dose will influence the roughness of the sidewall and the resistance to ion milling, and should be optimized for different fabrication flows, as will be discussed in Section 3.4.3.

After exposure and development, the sample is dry-etched via IBE (Oxford Ionfab 300 Plus) with only Ar⁺ plasma. The Ar⁺ gas flow used for plasma generation is 6 sccm. A higher concentration of Ar⁺ plasma will lead to a higher etching rate. The generated Ar⁺ plasma is accelerated via an electric field and directly bombards the LN surface. The pure physical etching process results in poor selectivity (around 1.4). The measured etching rate of LN is around 14 nm/min. During the etching process, especially for fully etched waveguides, we observe strong thermal accumulation that can cause local burning of the resist even with helium cooling. We therefore adopt a strategy to keep the temperature at a low level, which will be discussed in Section 3.3.2. Finally, the sample is sent for another run of solvent and standard cleaning to remove the remaining resist and by-products.

3.1.2 Fabrication steps for electro-optic modulators

EO modulators in LN play an important role in modern data communication links. On the basis of our ultralow-loss waveguides, we also developed a fabrication technique for EO modulators.

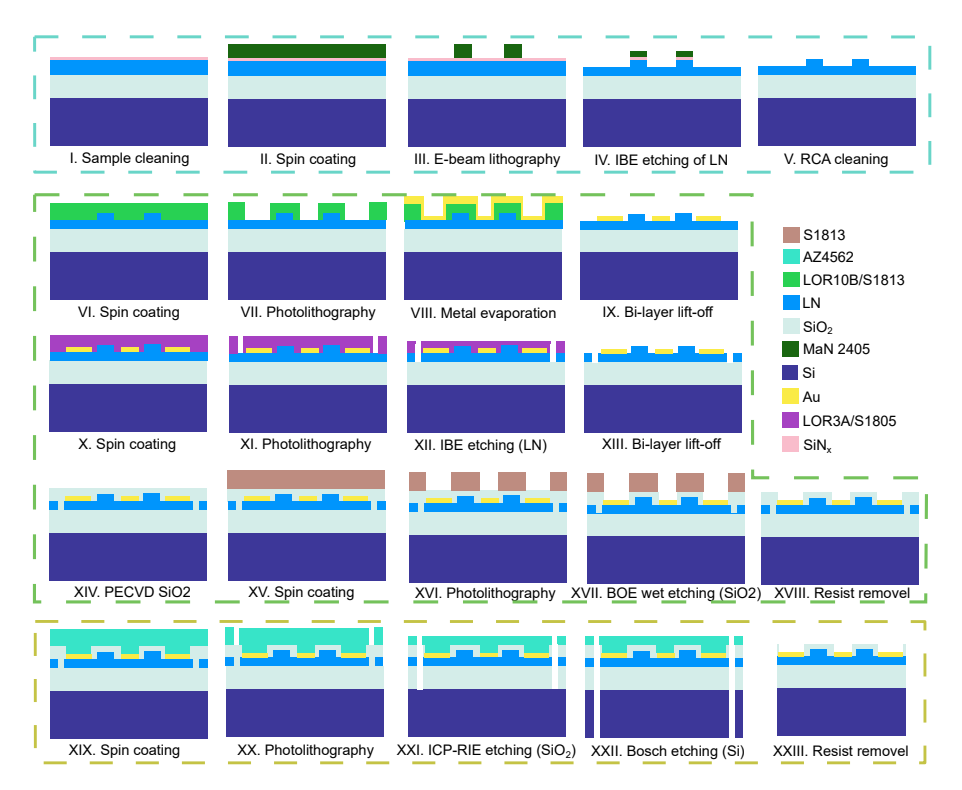


Figure 3.2: Schematic diagram of fabrication flow for ultralow-loss LN EO modulators. The blue dashed boxes (steps I to V) are the work flows for partially etched LN waveguides. Note in our fabrication flow, the recipe used for partially etching is the same as the recipe for fully etching in Fig. 3.1, but with different etching time. The green box (steps VI to XVIII) is the work flow mainly for thick electrodes fabrication in LN modulators. The yellow box is the work flow mainly for the facet etching, including LN slab (steps VI to XIII), SiO_2 and Si etching (steps XIX to XXIII).

The fabrication flow for LN EO modulators is shown in Fig. 3.2. For EO devices, the fabrication steps for the optical component are the same as the fabrication steps depicted in Fig. 3.1. In Fig. 3.2, the blue dashed boxes (steps I to V) are the work flows for partially etched LN waveguides. The green box (Steps VI to XVIII) is the work flow mainly for the thick electrode. And the yellow box (steps XIX to XXIII) is the work flow for the facet fabrication, including SiO₂ and Si etching.

After step V, the sample is spin coated with bilayer lift-off resists LOR10B/S1813, and photolithography is used to pattern the electrodes. Ti/Au (5/1200 nm) are then deposited via vacuum evaporation, and a lift-off process is performed to transfer the electrode pattern onto the

metal layer. Another spin coating with LOR3A/S1805 and photolithography is used to define the mask for the LN slab etching, in preparation for the facet etching. Then another ion beam etching is adopted to remove unnecessary LN slab. The recipe used for LN slab etching is the same as the recipe for LN waveguide etching. The sample is then cleaned and deposited with SiO₂ by plasma-enhanced chemical vapor deposition (PECVD). A new run of spin coating/photolithography/wet etching is used to define the patterns for probs contacting windows for LN modulators. A spin coating/photolithography run followed by inductively coupled plasma reactive etching (ICP-RIE) is then performed to define the chip facets masks (SiO₂ layer). Finally, the last coating/photolithography run followed by Bosch etching is performed for the etched facts (Si layer).

3.2 Electron beam lithography

We use EBL to define waveguide patterns. EBL is a high-precision nanofabrication technique that uses a focused electron beam to directly write nanoscale patterns on a resist-coated substrate [81,82]. With a resolution capability down to a few nanometers, EBL surpasses the limits of conventional optical lithography. The maskless operation of EBL makes it perfect for university research and the fabrication of industrial prototypes.

However, in contrast to conventional optical lithography which can expose large areas in a single exposure run, EBL is a shot-by-shot exposure process, which limits mass production. For EBL, the dwell time (t_{point}) of a single exposure shot can be determined by dose D (the electron energy deposited per unit of area), electron beam current I_E , and the exposure area A_{point} . The single shot cover area is determined by the beam step size (BSS, the distance between adjacent shots) and $A_{point} = BSS^2$. Therefore, we have

$$t_{point} = \frac{D \cdot BSS^2}{I_E}. (3.1)$$

The total exposure time is

$$t_{total} = N * t_{point} = \frac{A}{BSS^2F}, \tag{3.2}$$

where A is the total pattern area and N is the number of shots, and

 $N = A/BSS^2$. F is the writing frequency of the electron beam and $F = 1/t_{point}$.

For a given pattern, A is already determined and the BSS is usually chosen to be small enough to avoid jagged edges in patterns. However, a small BSS will significantly increase exposure time. Therefore, in this thesis, depending on the exposure pattern area, we choose different BSS to balance the exposure time and the pattern quality. In [Paper A], we used a BSS of 2 nm, and in [Paper B, E], we used a BSS of 3 nm. According to [83], a higher writing frequency combined with a small BSS provides lower optical losses. Therefore, once the BSS and dose is determined, we follow this principle to choose a beam current I_E that can achieve the largest writing frequency F (for Raith 5200, the maximum F is around 100 MHz).

Numerous electron beam shots need to be arranged carefully to increase the exposure efficiency and quality. In EBL, the deflection system is used to support the arrangement of electron shots. Starting from a graphic data system (GDS), the pattern to be exposed is first converted in machine language by specialized software such as Beamer (GenISys) and divided into sub-layouts: the writing fields (WFs). The WFs indicate the maximum cover range of the electron beam from the field deflection without physical movement of the sample. In Raith EBPG 5200, the WF can range from $160\times160~\mu\text{m}^2$ to $1024\times1024~\mu\text{m}^2$. The WF is then fractured into a smaller trapezoidal region (the so-called subfield) that is scanned and exposed by the electron beam with fine control. In each WF, the main field deflection is used to position the coordinate center of every subfield. In each subfield, the subfield deflection is used to achieve a shot-by-shot positioning of the electrons to cover the whole subfield region.

3.3 Ion beam etching

As discussed in Chapter 1, LN is a "hard" material to etch, with high hardness and good chemical stability. The commonly used reactive-ion etching (RIE) process in which a chemical reaction is involved is not suitable for LN etching. The first ultralow-loss LN waveguide was demonstrated in 2017 [29] using a pure physical etching method: ion beam etching (IBE) also called ion milling via Ar⁺. Note that some works [29, 84, 85] use the ICP-RIE tool to etch LN while only Ar⁺ is used and those works still belong to the pure physical etching method.

Chapter 3. Fabrication techniques for ultra-low loss lithium niobate waveguides

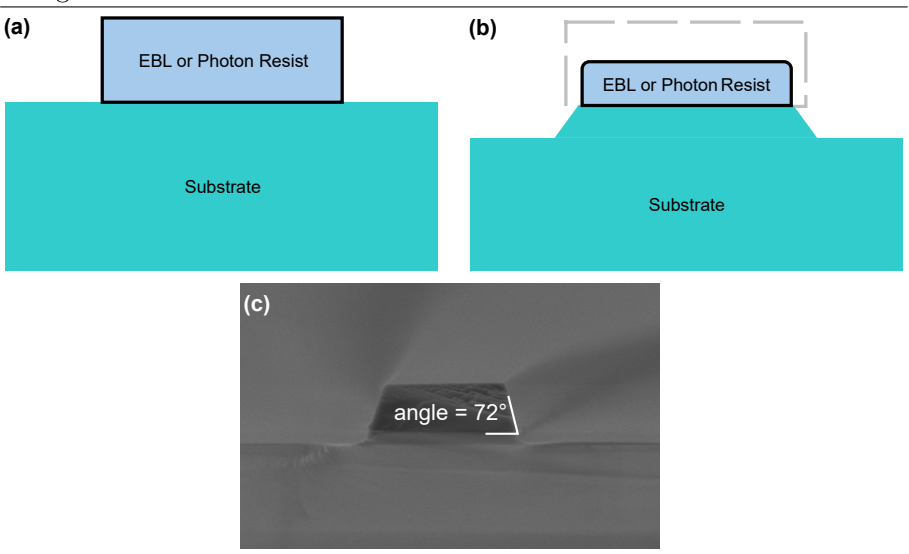


Figure 3.3: (a), (b) Schematic diagram of the profile evolution of resist and target substrate in IBE. (c) A typical fabricated LN waveguide with sidewall angle of 72 degree.

IBE is a pure physical etching process, and there is no chemical reaction to enhance the etching rate. The inert gas argon is introduced into an ion source and ionized, creating Ar⁺ plasma. The Ar⁺ plasma is collimated and accelerated through an external electric field. The high-energy Ar⁺ plasma then directly bombards the sample surface and removes the target materials by sputtering. The pure physical process leads to a non-selective etching (the etching rates for most of the target materials and masks are quite close). In contrast to RIE, IBE allows one to change the substrate angle, which changes the ion incident angle. The IBE etching rate and profile evolution are sensitive to the incident angle and usually need to be optimized. An improper choice of incident angle can lead to unwanted evolutions of waveguide profiles, such as cone growth [56]. In ion beam etching, the etched device always features a tilted sidewall angle; this is due to lateral etching of the resist. As shown in Fig. 3.3, during etching, partially scattered or incident ions with a non-vertical angle will etch the resist from the lateral direction and lead to "shrinking" of the resist. Depending on the etching rate of the substrate material in the vertical direction and the etching rate of the resist in the horizontal direction, a tilt angle will form in the substrate material. Our fabricated waveguides usually have a sidewall angle of 72°,

as shown in Fig. 3.3(c).

3.4 Challenges

3.4.1 Adhesion issues between LN and ma-N 2405

In Section 3.1, we mention that the sample is first sputtered with SiN_x before spin coating to promote adhesion between LN and ma-N 2405, which is due to the bad adhesion between LN and ma-N 2405. Commonly used adhesion promoters such as hexamethyldisilazane (HMDS) or Ti-prime do not provide enough adhesion between LN and ma-N 2405. Therefore, we introduce a "fake" adhesion layer by sputtering a thin layer of SiN_x on top of LN, and the adhesion between SiN_x and ma-N 2405 can be simply promoted by using HMDS. As shown in Fig. 3.3, the pattern is destroyed without the SiN_x layer, while the pattern survives with the SiN_x layer. To avoid the influence of sputtered SiN_x on the LN waveguide mode, the thickness of sputtered SiN_x is set to only a few nanometers. Using atomic force microscopy (AFM), we measure the surface roughness of the sample after SiN_x deposition, and the measured root mean square roughness (RMS) is around 0.5 nm which is comparable to the pure LN surface roughness (around 0.3 nm).

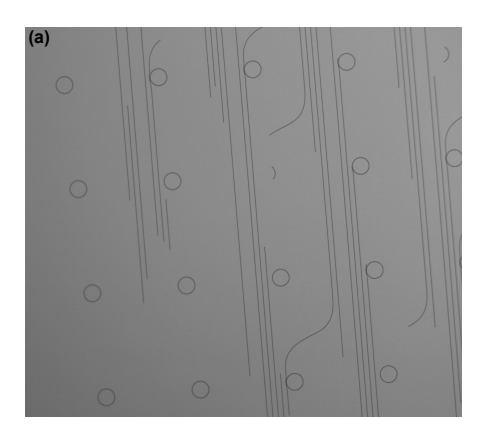




Figure 3.4: Microscope image for the fabricated waveguides (a) without SiN_x adhesion layer and (b) with SiN_x adhesion layer.

3.4.2 Heat accumulation during etching

Because of the high ion energy in the IBE process, the local temperature will accumulate to a high level that can even burn the resist. This was

observed for both photon resist S1813 and EBL resist Ma-N 2405.

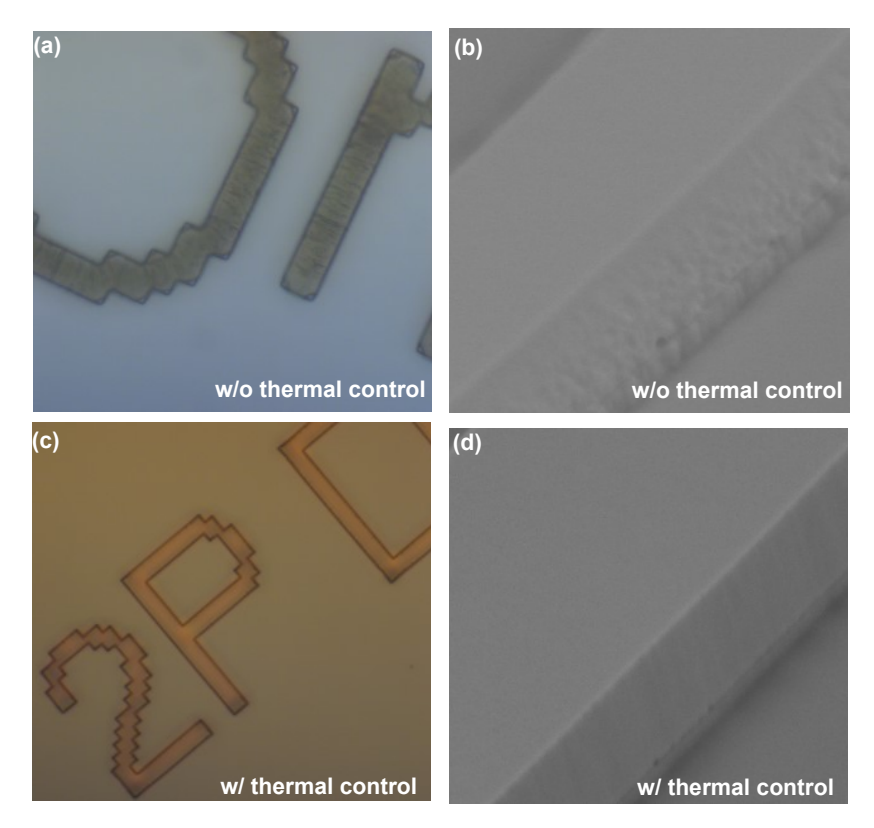


Figure 3.5: (a) Microscope image for the fabricated device without thermal control, the image was taken after dry etching by using Ma-N 2405 but before SC1 cleaning; (b) SEM images for the same device but performed RCA cleaning to remove resist residuals; (c), (d) Similar images but for the sample with thermal control.

Fig. 3.5 (a) shows a fully etched LN device without special treatment, the image was taken after dry etching but before SC1 cleaning. Black defects are clearly seen even in the low magnification microscope image. Fig. 3.5 (b) shows the SEM image for the same sample, but after cleaning (so we can see the LN waveguide profile clearly). The waveguide sidewall roughness is extremely large and there is a clear trend that the surface roughness increases significantly with the deeper etch depth, which is indirect evidence showing that the heat accumulated during the etching. The sample was etched continuously to the depth of 600 nm and the chip was placed on top of a silicon carrier wafer with a 120 degree thermal

tape during etching. Heat accumulation will lead to an extremely rough sidewall surface, and special treatments are required. Here we introduce several steps for thermal control: 1) choose a thermally stable resist (ma-N 2405 is a good example); 2) use thermal release tape between sample and carrier wafer; 3) perform etching-pause-etching cycling to allow the self-cooling of the sample; 4) use the largest amount of Helium cooling gas. By applying the above thermal control methods, we successfully suppressed the heat accumulation issues (Fig. 3.5(c)), and a smooth waveguide sidewall was obtained (Fig. 3.5(d)).

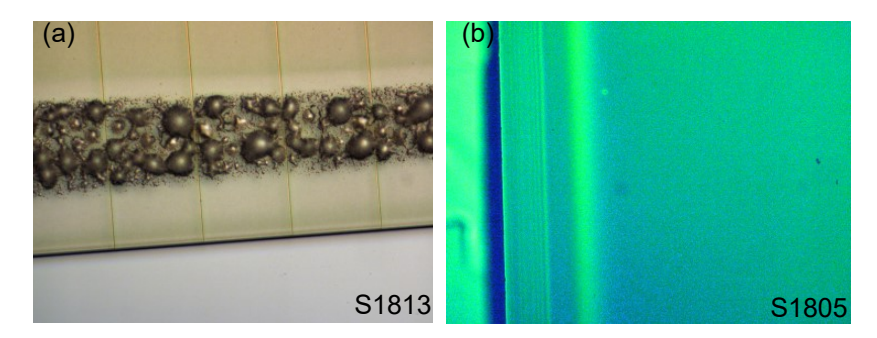


Figure 3.6: Microscope images for the fabricated devices after dry etching by using photon resist (a) S1813 and (b) S1805.

We also tried to use photon resist S1813 to etch LN, which is a convenient way for low-quality patterns like the facet etching in step XIII in Fig. 3.2. The accumulation of heat still occurs even though we used all of the thermal control methods mentioned above (Fig. 3.6(a)). Fortunately, we found that the heat accumulates much faster for thicker resists, and the heat issues are almost gone for a thinner resist S1805 (the same series), as shown in Fig. 3.6(b).

3.4.3 Resist resistance and dose optimization

In Section 3.1.1, we mentioned that the dose should be optimized on the basis of the sidewall roughness and the resist resistance. This must be considered especially for coupled waveguides with small gaps, such as the mirroring resonators (bus-ring coupled region) in [Paper A]. In the coupled region, higher-order effects of ions (reflection, scattering) become significant and will cause several etchings to the waveguide sidewall, leading to visible defects (shown in Fig. 3.7(a)). This issue can be solved by increasing the resist etching resistance (by increasing the exposure dose). A higher dose is used and no visible defects can be seen as shown in Fig. 3.7(b). However, a larger dose usually leads to an increased sidewall roughness for isolated waveguide. As a result, the dose need to be optimized by considering the balance of low sidewall roughness and high resist resistance. For mirroring resonators in [Paper A], the optimized dose is 270×2 ("2" indicates a dual-pass) $\mu\text{C/cm}^2$, and for spirals [Paper B], SBS waveguide [Paper E], modulators, the optimized dose is 230×2 $\mu\text{C/cm}^2$.

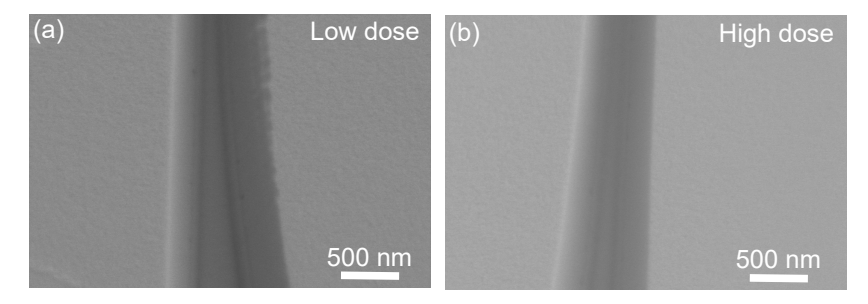


Figure 3.7: SEM images for the bus-ring coupled region for different doses, both images are taken udder 80 000x magnification.

3.4.4 Others

Except for above challenges, there are some other issues that need to be considered for ultra-low loss LN waveguides. The IBE will lead to relatively strong re-sputtering and generate byproducts that are difficult to remove. Based on our study, these byproducts can be effectively removed by SC1 cleaning. We also believe that oxygen plasma cleaning is a bad idea for resist removal (Ma-N 2405) and it will lead to extremely "hard" residuals that cannot be removed even with SC1 cleaning.

Chapter 4

Third-order nonlinear applications in lithium niobate

As mentioned in Chapter 2, LN is notorious for its large second-order nonlinearity and a wide transparency window, combined with a moderate third-order nonlinearity. Thanks to recently developed nanofabrication methods, ultralow-loss LN waveguides with loss down to a few dB/m have been demonstrated. The significant reduction of linear losses makes LN a promising waveguide platform that can achieve ultra-broadband nonlinear processes at moderate pump power. In this chapter, we focus on third-order nonlinearities and the corresponding applications in supercontinuum generation (SCG) and Kerr comb generation (KCG).

4.1 Dispersion engineering

Dispersion is one of the most important properties of optical waveguides, which describes the wavelength/frequency dependency of the propagation constant. Dispersion engineering is crucial for many nonlinear applications. Due to advanced nanofabrication with high precision control of waveguide geometry, precise dispersion engineering in LNOI is possible and has been first demonstrated in [86]. Flexible dispersion control was used for applications such as KCG [30,31] and SCG [87,88].

The propagation constant β is a function of the angular frequency ω ,

which can be expressed as a Taylor series:

$$\beta(\omega) = \beta_0 + \beta_1(\omega - \omega_0) + \frac{1}{2}\beta_2(\omega - \omega_0)^2 + \frac{1}{6}\beta_2(\omega - \omega_0)^3 + \cdots$$
 (4.1)

where $\beta_0 = \beta(\omega_0)$ is the propagation constant at frequency ω_0 , $\beta_1 = \frac{d\beta}{d\omega} = \frac{1}{v_g}$ is the group delay, $\beta_2 = \frac{d^2\beta}{d\omega^2}$ is the group velocity dispersion (GVD) term and $\beta_n (n \geq 3) = \frac{d^n\beta}{d\omega^n}$ are the higher order dispersion terms. For many cases, higher-order dispersion can be neglected, and GVD is the dominant dispersion. However, for near-zero GVD, higher-order dispersion will be significant and needs to be considered.

There are two different types of dispersion in optical waveguides: material dispersion and geometric dispersion. Material dispersion refers to the refractive index of the material that depends on the optical frequency. The material dispersion is determined by material properties, but can also be changed via altering the waveguide geometry (control the light distribution among the core and cladding area). Geometric dispersion refers to the waveguide geometry-induced mode effective index change, which is also called mode dispersion. The two dispersions are independent; for example, even there is no material dispersion, geometric dispersion can still exist.

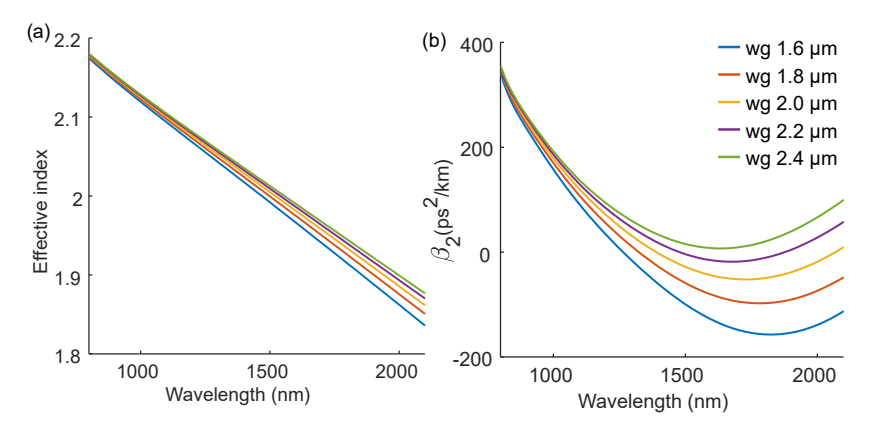


Figure 4.1: (a) Simulated mode effective index for different waveguide widths; (b) Simulated GVD for different waveguide widths. The waveguide is fully etched and the top cladding is air. The LN total thickness is 580 nm, the sidewall angle of is 70°, and the LN ordinary material refractive index is used.

GVD curves can be generated by numerically simulating the effective waveguide mode index and extracting the second derivative. Using

an FEM solver, we calculated the effective index of the mode and the calculated GVD, as shown in Fig. 4.1. The waveguide GVD can be tailored by carefully changing the waveguide geometry: width, thickness, angle. By choosing proper geometric parameters, a near-zero dispersion (GVD \sim 0), normal dispersion (GVD>0), and anomalous dispersion (GVD<0) can be achieved. For LN curved waveguides with a bending radius of a few tens of μ m, the waveguide mode is different from the mode in straight waveguides, which will significantly affect the GVD of the waveguide. In Fig. 4.2, we calculated the mode effective index and GVD for a straight waveguide and compared it with a curved waveguide with the same geometric parameters but with a bending radius of 40 μ m. Bending the waveguide tends to increase the GVD over the simulated wavelength range, and the GVD change is as high as \sim 70 ps²/km at 1550 nm,

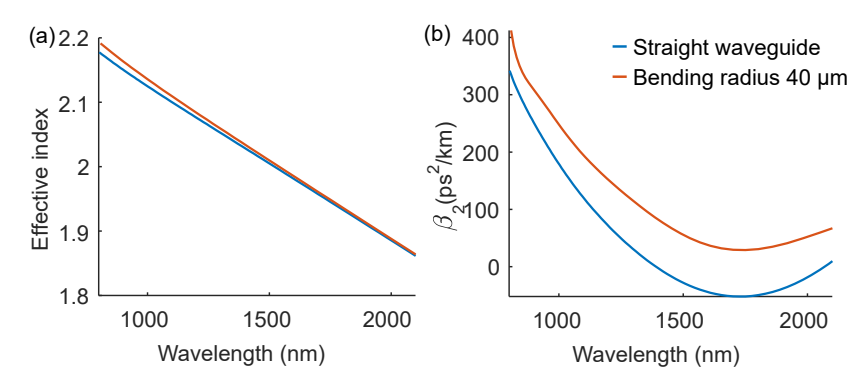


Figure 4.2: (a) Simulated mode effective index considering bending radius; (b) Simulated GVD considering bending radius. The waveguide is fully etched and the top cladding is air. The LN total thickness is 580 nm, the waveguide width is 2 μ m, the sidewall angle of is 70°, and the LN ordinary material refractive index is used.

4.2 Supercontinuum generation

SCG is a technique for generating ultrabroad spectra with high coherence and brightness, where an intense input laser pulse is broadened in nonlinear media through nonlinear interactions. SCG was first observed in bulk glass [89] and then has been investigated in different media, including solids, liquids, and gases. SCG strongly depends on the linear and nonlinear properties of the medium. In the early years, dispersion engineering capabilities and the reduction of the core area of photonic crystal fibers

(PCF) enabled the demonstration of SCG with enhanced performance compared to SC from bulk or conventional silica fibers [90]. In recent decades, SCG has also been demonstrated in many integrated platforms, including Si [91], SiN [92], AlGaAs [93], AlN [94], and LN [87,88]. There are a few advantages for SCG in integrated waveguides, such as further enhanced light field confinement, lower power consumption, and potential for dense integration with additional functionalities [95].

SCG in LN waveguides possesses a few unique advantages due to the large χ^2 and moderate χ^3 nonlinearities, which allows one to generate SC and second harmonic (SH) in the same LNOI waveguide. SH and SC can provide a very simple and direct detection of the self-referencing beatnote with conventional photodiodes [88, 96, 97]. Other work focused on the extension of the SC spectrum bandwidth to visible and ultraviolet areas by exploiting χ^2 nonlinearities [98, 99].

SCG involves a process with high-power pulse propagation inside a nonlinear waveguide. If we solely consider χ^3 nonlinearities (a detailed investigation for considering both χ^2 and χ^3 can be found in [100]), and assume the slowly varying envelope approximation, then pulse propagation can be described by the nonlinear Schrödinger equation (NLSE) [101]:

$$\frac{\partial A}{\partial z} = -\frac{\alpha}{2}A + \sum_{n\geq 2} \frac{i^{n+1}\beta_n}{n!} \frac{\partial^n A}{\partial t^n} + i\gamma |A|^2 A, \tag{4.2}$$

where

$$\gamma = \frac{3\chi^{(3)}\omega_0}{8n_0c} \frac{\iint |F(x,y)|^4 dx dy}{\iint |F(x,y)|^2 dx dy},$$
(4.3)

The NLSE Eq. 4.2 is written without β_1 using a co-moving reference frame with the pulse group velocity $v_g = 1/\beta_1$ [101]. Eq. 4.2 describes the pulse envelope (A) evolution along propagation distance (z) (ignoring Raman and higher-order nonlinear effects), which depends on the Kerr nonlinear effect (γ) , the dispersion (β_n) , and the propagation loss (α) .

The spectral broadening is strongly dependent on the waveguide dispersion and its interplay with nonlinearities as different physical phenomena can occur. Depending on the dispersion sign at the pump wavelength, there are two different types of SCG: SCG in the anomalous dispersion regime and SCG in the all-normal dispersion (ANDi) regime.

Most SCGs work in anomalous dispersion, where solitons are supported by the opposite effects of self phase modulation (SPM) and GVD. For SCG, usually high-order solitons can be generated, and the initial

spectral broadening caused by SPM and subsequent temporal compression are proportional to the soliton number N. The dramatically broadened high-order soliton will usually be perturbed and leads to soliton fission [102], so that N fundamental solitons split from the high-order soliton in time. Together, these fundamental solitons cover a much broader spectrum. Moreover, leveraging dispersive wave emission allows one to further broaden the spectrum. Usually, pumping at low anomalous dispersion allows one to maximize the number of solitons, and therefore to broaden the spectrum. However, the process is dependent on modulation instability (MI), and the unseeded MI gain can amplify the noise of the input pulse [103], which may limit the coherence of the resulting pulse.

An alternative approach is to work in the ANDi regime. When a pulse propagates at normal dispersion, the main mechanism for spectral broadening is SPM. Since the chirps imposed on the spectrum by normal dispersion and by SPM have the same sign, the spectral broadening is limited within the relatively narrow regime. The interaction between GVD and SPM in the normal dispersion regime causes optical wave breaking (OWB) [104]. At the beginning of the propagation, SPM leads to a frequency chirp imposed on the pulse with a typical S-shape. GVD leads to a further steepening at the edges of the pulse spectrum. After a specific distance of propagation, the red-shifted components near the pulse leading edge travel faster and overtake the slower preceding tail (the opposite happens for the blue-shifted wavelengths at the trailing tail), resulting in OWB. The OWB leads to a significant enhancement of spectrum flatness and a nearly linear distribution of the instantaneous frequency across the pulse duration. Since SPM and OWB generation are much less susceptible to noise amplification compared to soliton dynamics in anomalous dispersion, SC in ANDi waveguides has higher phase stability and coherence [105]. We demonstrated SCG in ANDi LN waveguides and achieved an octave-spanning SC comb in [Paper B].

4.3 Kerr-comb generation in LN microresonators

Another approach for broadband frequency comb in an integrated platform is KCG implemented in passive high-Q microresonators [106]. Unlike SCG, in KCG, a continuous-wave (CW) laser instead of a pulsed laser is usually used to pump one of the resonant modes and produces MI gain via four-wave mixing (FWM) in other resonant modes [107,108]. Optical parametric oscillation based on the Kerr effect in microresonators was first reported in [107,108]. In these works, high Q microresonators were used to allow the generation of frequency combs with low threshold pump power. A special form of frequency comb in microresonators is the dissipative Kerr soliton (DKS), which was first demonstrated in [109]. In optical fibers, soliton relies on the balance between dispersion and nonlinearity. In microresonators, DKS is dependent not only on the balance between dispersion and nonlinearity, but also on the extra balance between optical loss and gain [110]. DKS has been demonstrated on numerous integrated waveguide platforms, such as Si_3N_4 [24,111], SiO_2 [112], AlN [113], and LN [30,31].

DKS can be described using the Lugiato-Lefever equation (LLE), which is also known as an externally driven, damped NLSE. The LLE can be expressed as:

$$t_R \frac{\partial A}{\partial \tau} = (\alpha - i\delta_0 - \frac{iL\beta_2}{2} \frac{\partial^2}{\partial t^2} + iL\gamma |A|^2) A + i\sqrt{\theta} A_{in}, \qquad (4.4)$$

where t_R is the roundtrip time, θ is the coupling coefficient between the bus and the ring waveguides, τ is the slow cavity time, and $\alpha = -\frac{\theta + \alpha_i L}{2}$ describes the total cavity losses, δ_0 is the detuning parameter, and A_{in} is the incident pump field.

With the fast development of ultralow-loss LN waveguides, LNOI has been considered to be a particularly promising platform for DKS. Due to its capability of hosting an entire photonic circuit on a single chip, including: SHG, DKS, and EO modulator. However, DKS in LN is not simple due to the strong Raman effect that will compete with comb generation [58]. The Raman effect is strongest when the light is polarized along the z-axis of the crystal. Most DKS are based on the Z-cut LN platform with TE mode to avoid the large Raman effect on the LN z-axis. Very recently, two similar works also demonstrated smooth soliton micocombs in X-cut LN by using a racetrack resonator with a large straight waveguide fraction aligned along the z-axis to reduce the effect of the strong Raman effect [59,114]. By using the high-Q and ultra-small Z-cut LN ring resonators, [Paper A] demonstrated a 500 GHz repetition rate DKS.

Chapter 5

Efficient electro-optic modulators in lithium niobate

As one of the most important applications in LN, EO modulators play a key role in numerous fields, including optical communication, microwave optics, quantum optics, etc., where they efficiently encode electrical signals onto optical carriers [11,67,115,116]. LN modulators have attracted significant research interest in the past few decades due to the unique material properties of LN, such as its strong EO coefficient, low optical losses, and a high refractive index [29, 32, 34, 35, 38, 117, 118]. With the rapid development of the ultralow-loss integrated LN waveguide platform, on-chip LN EO modulators have attained great research interest in both academia and industry [48,61,62,119,120]. Today, state-of-the-art integrated LN modulators can simultaneously achieve large bandwidth operation (>100 GHz) and low drive voltage (< 1 V), making them indispensable for next-generation photonic systems.

In this chapter, we will briefly introduce the working principle of LN EO modulators and discuss the design rules for achieving high-performance modulators especially for large EO bandwidth and high modulation efficiency.

5.1 Electro-optic modulator

A typical EO phase modulator operates by electrically altering the real part of the waveguide's refractive index via the EO effect (also called the Pockels effect), thereby modulating the optical phase. As illustrated in Fig. 5.1(a), an applied drive voltage induces an external electric field

across the optical waveguide, altering its refractive index. Intensity modulation can be obtained from phase modulation by interfering light in two phase-modulated waveguides constructively or destructively. Fig. 5.1 (b) depicts a conventional Mach-Zehnder interferometer (MZI) based intensity modulator, in which the light will be coupled to two separate waveguides via a 3 dB coupler and recombined after the modulation region. The external voltage is then applied on the center electrodes, generating opposing electric fields in the two waveguides. Consequently, the waveguides accumulate phase changes of opposite signs—a "push-pull" configuration that effectively reduces the required drive voltage by half. This "push-pull" design approach is used in nearly all LN MZI-based intensity modulators.

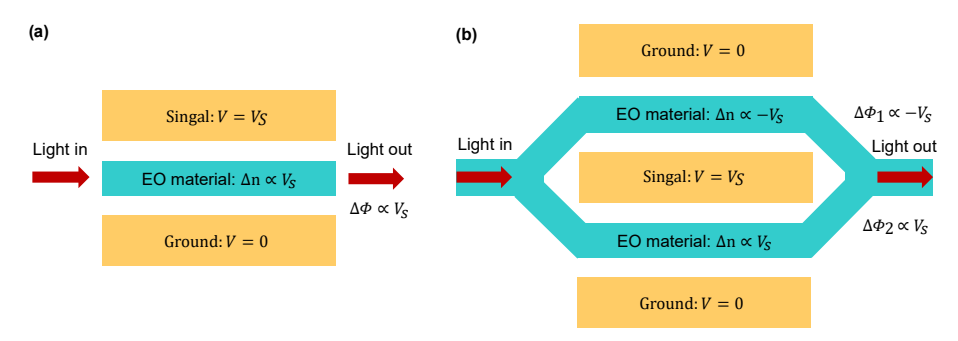


Figure 5.1: The principle of (a) phase and (b) intensity electro-optic modulators.

5.2 Electro-optic effect in lithium niobate

The linear EO effect (Pockels effect) is a special second-order nonlinear optical process, where the material refractive index is varied proportionally to an externally applied electric field (pump wave frequency is DC - a few hundreds GHz). The EO effect is different from the all-optical nonlinear effect where the pump wave frequency is an optical frequency.

As we discussed in Chapter 2, LN is an anisotropic uniaxial crystal and the relative permittivity of the material is a tensor. If we use Arabic numerals (1, 2, 3) to represent the coordinates (x, y, z) in a Cartesian coordinate system, and align the LN crystal extraordinary axis to be z, ordinary axes to be x, y, then the material's relative permittivity tensor can be expressed as a 3×3 matrix:

$$\boldsymbol{\epsilon_r} = \begin{bmatrix} \epsilon_{11} & 0 & 0 \\ 0 & \epsilon_{22} & 0 \\ 0 & 0 & \epsilon_{33} \end{bmatrix}, \tag{5.1}$$

where

$$\epsilon_{11} = \epsilon_{22} = n_o^2, \epsilon_{33} = n_e^2.$$
 (5.2)

Due to the EO effect, the elements of the relative permittivity matrix ϵ_{ij} (i, j = 1, 2, 3), are functions of the applied RF field components E_k (k = 1, 2, 3):

$$\Delta \frac{1}{\epsilon_{ij}} = \sum_{k=1}^{3} r_{ijk} E_k. \tag{5.3}$$

Here, only the dominant linear EO effect (Pockels effect) is considered, and the quadratic and higher-order effects are ignored.

$$\Delta \frac{1}{\epsilon_{ij}} = \Delta \frac{1}{n_{ij}^2} \approx -\frac{2}{n_{ij}^3} \Delta n_{ij}, \tag{5.4}$$

We then get

$$\Delta n_{ij} \approx -\frac{n_{ij}^3}{2} \sum_{k=1}^3 r_{ijk} E_k.$$
 (5.5)

Here r_{ijk} are elements of the linear EO tensor \mathbf{r} (dimension $3 \times 3 \times 3$, 27 components). The linear elements of the EO tensor in LN satisfy reciprocity due to the symmetry of its permittivity tensor, which implies $r_{ijk} = r_{jik}$, so only 18 elements must be considered in \mathbf{r} . To simplify the notation, we introduce subscript l (l = 1, 2, 3... 6), to replace the subscript ij, according to the rule:

ij	11	22	33	23,32	31,13	21,12
ij	XX	уу	$\mathbf{Z}\mathbf{Z}$	$_{\rm yz,zy}$	$_{\rm zx,xz}$	yx,xy
l	1	2	3	4	5	6

Then equation 5.5 becomes:

$$\Delta n_l \approx -\frac{n_l^3}{2} \sum_{k=1}^3 r_{lk} E_k. \tag{5.6}$$

For LN, due to crystal symmetry, most of the elements in ${\bf r}$ are zero. The only non-zero terms are:

$$r_{13} = r_{23} = 9.6 \,\mathrm{pm/V}$$

 $r_{33} = r_{51} = r_{42} = 30.9 \,\mathrm{pm/V}$
 $r_{22} = -r_{12} = -r_{61} = 6.6 \,\mathrm{pm/V}$. (5.7)

If we apply an external electric field along the z axis ($E_1 = E_2 = 0$, $E_3 = E_{el}$) and assume that E_{el} is uniformly distributed throughout the EO material, the changes in the refractive indices of LN are:

$$\Delta n_{xx} = \Delta n_{yy} = \Delta n_o = -\frac{n_o^3 r_{13}}{2} E_{el}$$

$$\Delta n_{zz} = \Delta n_e = -\frac{n_e^3 r_{33}}{2} E_{el}$$

$$\Delta n_{xy} = \Delta n_{yz} = \Delta n_{xz} = 0.$$
(5.8)

With such a configuration, the extraordinary index (n_e) and the ordinary index (n_o) of LN will be changed simultaneously by applying E_{el} . However, n_e is altered by the largest EO coefficient r_{33} , while n_o is altered by a much smaller EO coefficient r_{13} (exact values of r_{33} and r_{13} can be found in Chapter 2). Therefore, to utilize the largest EO tensor r_{33} in integrated LN modulators, there are usually two configurations:

- (1) X-cut (Y-cut) configuration; see Fig. 5.2(a). In an X-cut (Y-cut) LN crystal, the light propagates along the y(x) direction. The electrodes are placed horizontally on two sides of the waveguide and the dominant external electric field is E_z . The optical mode used is the TE mode with mode polarization along the optical axis (z). Now both optical and electric fields are aligned along the z-axis of LN.
- (2) Z-cut configuration; see Fig. 5.2(b). In a Z-cut LN crystal, the light propagates along the y or x direction. The electrodes are placed to obtain a dominant electric field E_z around the optical waveguide, and usually the hot electrode can be placed on top of the waveguide. The optical mode used is TM mode so that the optical field is aligned along the same direction as the applied electric field.

Note here in both of the cases, we have the extraordinary refractive index change:

$$\Delta n_e = -\frac{n_e^3 r_{33}}{2} E_{el}. (5.9)$$

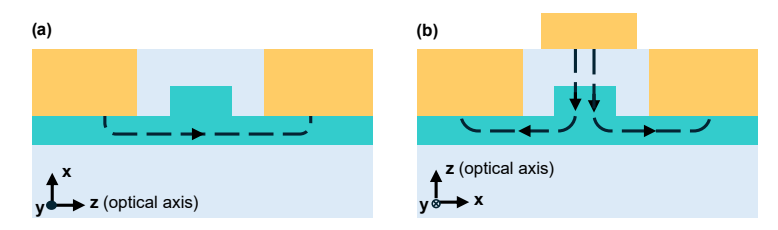


Figure 5.2: Two typical configuration of LN modulator: (a) X-cut, (b) Z-cut.

No matter which type of LN crystal is used, to utilize the largest EO tensor r_{33} , the extraordinary refractive index n_e must be used. This is not compatible with the preferred linear and χ^3 nonlinear cases (preferred to use an ordinary refractive index) as we discussed in Chapters 2 and 4.

5.3 Static electro-optic response

In the previous section, we discussed the EO response of the LN modulator by assuming uniform electric and optical fields. For a modulator, the optical and electric fields are not uniform, and the external electric field caused effective index change needs to be considered. It can be calculated from perturbation theory (here for the X-cut TE mode configuration) [121]:

$$\Delta n_{TE} = \frac{\iint E_{op}^2(z, x) \Delta n_e(z, x) dz dx}{\iint E_{op}^2(z, x) dz dx}.$$
 (5.10)

Substituting equation 5.9 into it, we get:

$$\Delta n_{TE} = -\frac{n_e^3 r_{33}}{2} \frac{\iint E_{op}^2(z, x) E_{el}(z, x) dz dx}{\iint E_{op}^2(z, x) dz dx}.$$
 (5.11)

where $E_{el}(z, x)$ is the electric field distribution due to the applied voltage V_0 on the electrodes. By setting the active region length to be L, the total phase change of the modulator is:

$$\Delta\phi(V_0) = \Delta\beta L$$

$$= \Delta n_{TE}\beta_0 L$$

$$= -\frac{n_e^3 r_{33}\pi L}{\lambda_0} \frac{\iint E_{op}^2(z, x) E_{el}(z, x) dz dx}{\iint E_{op}^2(z, x) dz dx}.$$
(5.12)

Now we use a normalized term $e_{el}(z, x)$ to replace the actual electric field $E_{el}(z, x)$ with the relation of:

$$e_{el}(z,x) = \frac{1}{V_0} E_{el}(z,x).$$
 (5.13)

Then the integral term in equation 5.12 will be independent of the applied voltage V_0 . And equation 5.12 becomes:

$$\Delta\phi(V_0) = -\frac{n_e^3 r_{33} \pi V_0 L}{\lambda_0} \frac{\iint E_{op}^2(z, x) e_{el}(z, x) dz dx}{\iint E_{op}^2(z, x) dz dx}$$

$$= -\frac{n_e^3 r_{33} \pi V_0 L}{\lambda_0} \Gamma.$$
(5.14)

Where Γ is the overlap integral:

$$\Gamma = \frac{\iint E_{op}^2(z, x) e_{el}(z, x) dz dx}{\iint E_{op}^2(z, x) dz dx}.$$
(5.15)

The Γ on the one hand represents the overlap between the optical and external electric fields, on the other hand, it represents the efficiency of the electrodes to generate electric field on the optical waveguide with unit voltage applied. Making $\Delta \phi(V_0) = \pi$, we then get the important figure of merit in LN modulators, the voltage length product $V_{\pi}L$, which is:

$$V_{\pi}L = -\frac{\lambda_0}{n_e^3 r_{33} \Gamma}. (5.16)$$

 $V_{\pi}L$ is an intrinsic figure of merit for LN modulators, where a smaller value corresponds to a more efficient modulation. A low $V_{\pi}L$ allows for sufficient modulation strength at reduced voltages and shorter device lengths. This parameter depends on three key factors: (1) material properties (refractive index, EO coefficient), (2) operating wavelength (λ_0) , and (3) cross-sectional dimensions of the electrodes for larger Γ . Selecting an EO material with a high EO coefficient and a large refractive index will lead to a smaller $V_{\pi}L$. For modulators with shorter wavelength, the $V_{\pi}L$ is smaller due to: (1) the explicit λ_0 dependence in equation 5.16 and (2) the ability to place electrodes closer together, increasing the overlap integral (Γ) . In practice, once the EO material and the operating wavelength are chosen, optimizing the modulator layout and geometric parameters becomes critical to achieve the lowest possible $V_{\pi}L$.

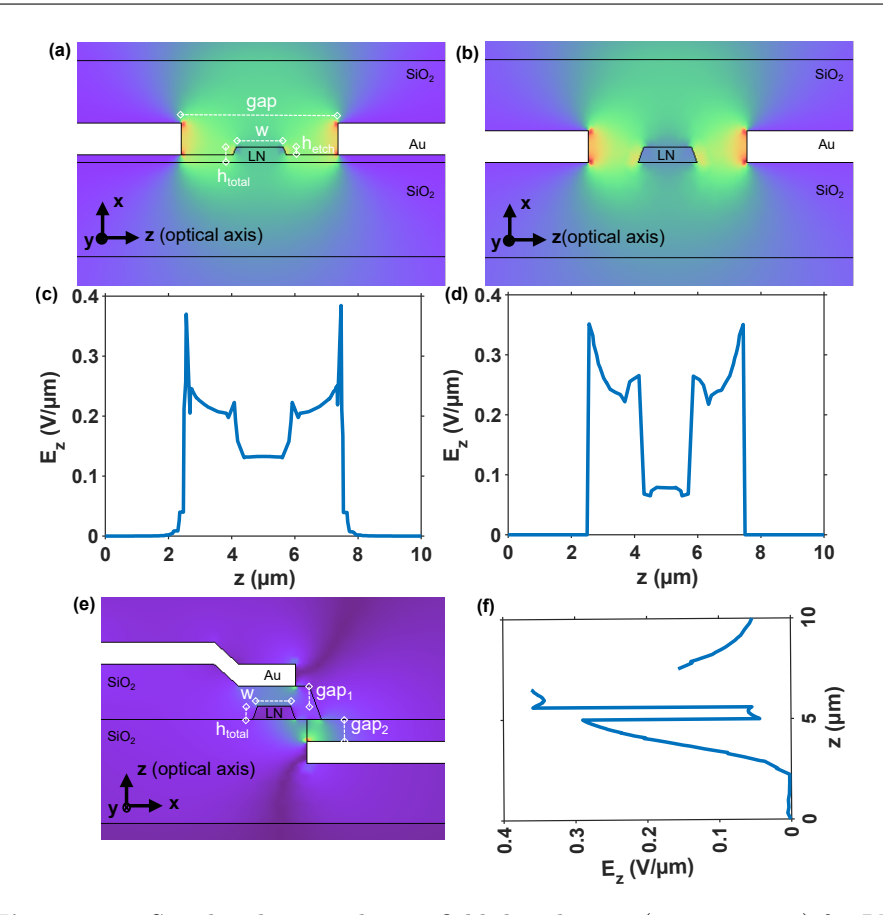


Figure 5.3: Simulated static electric field distribution (z-component) for LN modulators with 1 V voltage applied on electrodes. (a), (c) X-cut configuration with partially etched LN waveguide; (b), (d) X-cut configuration with fully etched LN waveguide; (e), (f) Z-cut configuration with fully etched LN waveguide. Parameters used in the simulation for X-cut configuration are: $[w, h_{etch}, h_{total}, gap] = [1.5, 0.25, 0.5, 5]$ µm, and for Z-cut are: $[w, h_{total}, gap_1, gap_2] = [1.5, 0.6, 0.9, 1]$ µm. The angle of LN waveguide sidewall is 70 degree. Note the coordinates are the same as the LN crystal axes, and we always plot E_z along the z-axis.

Fig. 5.3 shows three possible LN modulator layouts and the corresponding static electric field distribution (simulated by electrostatics, COMSOL Multiphysics [122]) with a 1 V applied voltage on the electrodes. They are: (1) X-cut configuration with a partially etched LN waveguide; (2) X-cut configuration with a fully etched LN waveguide; and (3) Z-cut configuration with a fully etched LN waveguide. Regardless of the chosen layout, an electric field "valley" consistently appears

in the waveguide core region. This phenomenon arises from the electromagnetic boundary conditions at the dielectric interfaces, which require continuity in the normal component of the electric displacement vector (\mathbf{D}) . Given the significant permittivity contrast between LN $(\epsilon_{LN} \approx 28)$ and SiO₂ $(\epsilon_{LN} \approx 4.2)$, the electric field within the high-permittivity LN core becomes substantially weaker than that of the surrounding cladding SiO₂. Using a partially etched waveguide (which can reduce the effective permittivity contrast), a decreased 'valley' depth can be achieved, and a smaller $V_{\pi}L$ can be obtained compared with the fully etched waveguide. As we discussed in Chapter 2, 4, a Z-cut LN waveguide platform features a few advantages both for linear and nonlinear applications. However, an efficient Z-cut modulator is challenging because electrode layouts can degrade the modulation efficiency. As shown in Fig. 5.3 (e), (f), the electric field in the LN core region is significantly reduced from around 0.35 V/µm to 0.05 V/µm.

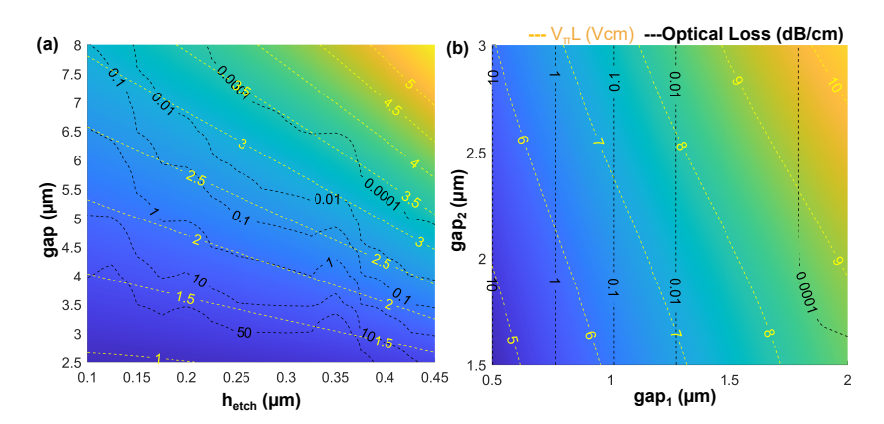


Figure 5.4: Optimization of the modulator $V_{\pi}L$ and the propagation loss. (a) Results for X-cut partially etched layout and (b) for Z-cut fully etched layout. The parameters used are from Fig. 5.3. Here the V_{π} is calculated in the case of push-pull configuration for a intensity modulator and the V_{π} for a single phase modulator should be twice of the calculated value.

As we discussed previously, optimizing the modulator geometry is necessary to obtain a small $V_{\pi}L$, and this generally requires us to move the electrodes closer to each other to increase the overlap factor Γ (like in a parallel plate capacitor, the electric field inside the two electrodes is nearly inversely proportional to the electrode distance). However, metallic electrodes placed near the optical waveguides will introduce significant optical loss. As a result, there is a trade-off between $V_{\pi}L$ and insertion

loss (IL, another key performance metric in LN modulators). As shown in Fig. 5.4, the $V_{\pi}L$ and IL optimization results show an opposite trend with the swept geometric parameters. And this will limit the minimum achievable $V_{\pi}L$ to around 2 V·cm in the X-cut partially etched configuration and to around 6 V·cm in the Z-cut fully etched configuration. The results further validate that the partially etched X-cut configuration can achieve the smallest $V_{\pi}L$. In the rest of this chapter, we consider the X-cut partially etched modulators unless otherwise specified. For this configuration, the 2 V·cm $V_{\pi}L$ means a few cm long electrodes are needed to get an $V_{\pi} < 1$ V and the device is relatively bulky.

5.4 Optical loss and plasmonic mode coupling

In the end of last Section, we introduced an important $V_{\pi}L$ -IL trade-off in EO modulators, which will limit the modulation performance. To reduce the modulator $V_{\pi}L$ and improve the modulator performance, most works focus on $V_{\pi}L$, while in this thesis we tried to break this trade-off from IL. We studied the source of metal-induced optical losses in the LN modulator and found that this loss is related to the mode coupling between the optical dielectric waveguide mode and metal-dielectric plasmonic (pl) modes [123,124].

The presence of metal electrodes in optical modulators introduces absorption losses in adjacent optical waveguides as a result of the substantial imaginary component of the metal's refractive index. This detrimental effect becomes particularly pronounced in integrated LN modulators because of their unique electrode configuration, which places the electrodes on top of a thin film LN slab. Figs. 5.5 (a)-(c) show typical cross sections of the LN modulator and the corresponding simulated optical mode profiles (Mode solver, COMSOL Multiphysics). The optical mode field is mainly distributed in the waveguide core region, while a small amount of light is distributed near the metal electrodes. From perturbation theory [125], the presence of metal electrodes could be treated as a small refractive index perturbation (both real and imaginary) in the optical mode (without metal). From another point of view, the metal-LN-SiO₂ sandwich structure (without dielectric waveguide) establishes a pl waveguide [126,127], which supports a family of pl modes, as shown in Figs. 5.5 (d)-(k). The pl modes confine light within the LN slab region beneath the metal electrodes. Therefore, the pl modes exhibit an effective index (n_{pl}) that is predominantly determined by the refractive index of the LN, resulting in values comparable to the effective index (n_{op}) of the optical modes in the waveguide. As a result, strong mode coupling occurs between these two waveguide systems, enabling significant energy exchange through evanescent-field interactions.

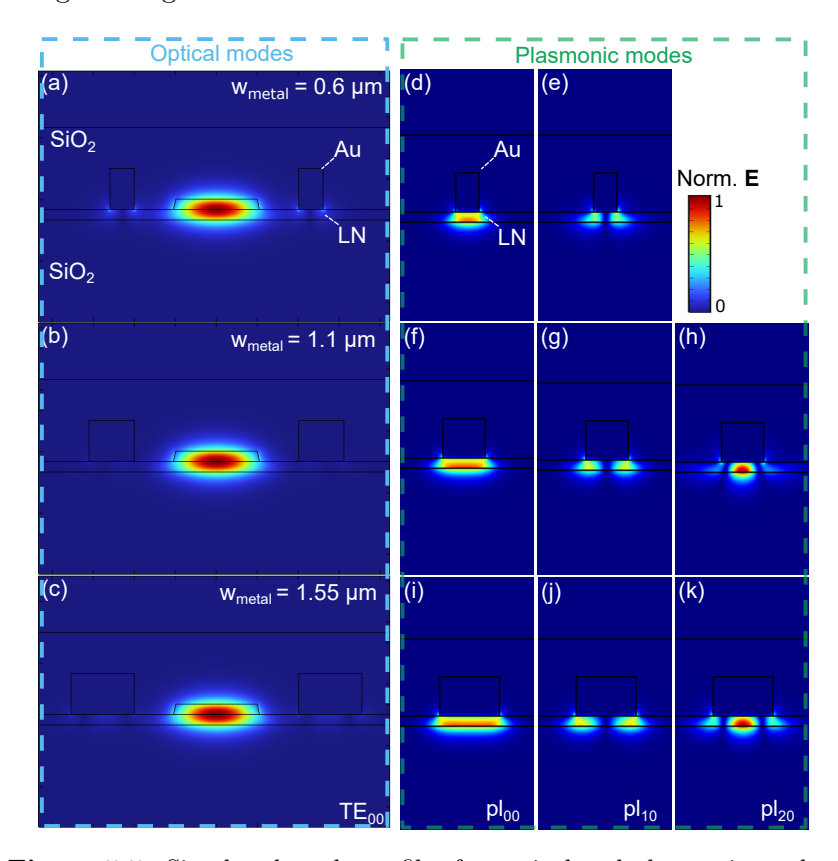


Figure 5.5: Simulated mode profiles for optical and plasmonic modes.

Now we will follow the mode coupling view to explain the optical loss in the LN modulator. The system is similar to a conventional directional coupler, but one of the coupled waveguides is lossy. This coupled system of two waveguides can be effectively analyzed using simplified coupled mode theory (CMT) with proper consideration of the metal's complex refractive index [124, 128]. The simplified coupled mode equations in a two-waveguide system with consideration of propagation loss is as follows:

$$\begin{cases} \frac{\mathrm{d}\mathbf{E}_{1}}{\mathrm{d}z} = i\left(\gamma_{1}\mathbf{E}_{1} + \kappa\mathbf{E}_{2}\right) \\ \frac{\mathrm{d}\mathbf{E}_{2}}{\mathrm{d}z} = i\left(\gamma_{2}\mathbf{E}_{2} + \kappa\mathbf{E}_{1}\right), \end{cases}$$
(5.17)

where γ_1 , γ_2 are the complex propagation constants for isolated modes in the two waveguides without coupling, and the E_1 , E_2 are the electric field in the optical and pl waveguide in the coupled system. The coupling coefficient κ can be obtained by: [129]:

$$\kappa = \frac{1}{4} \sqrt{\frac{\epsilon_0}{\mu_0}} \iint (n^2(x, y) - n_1^2(x, y)) \Phi_1^* \Phi_2 dx dy, \tag{5.18}$$

where n(x, y) and $n_1(x, y)$ are the refractive index distribution for the coupled system and the isolated optical waveguide, respectively. The Φ_1 and Φ_2 are the normalized electric field (the mode power is normalized to be 1 W) for isolated modes.

By solving equation 5.17, we could obtain the electric field distribution along the propagation direction, with initial condition: $E_1 = 1$, and $E_2 = 0$ (light input from the optical waveguide). The results are shown in Fig. 5.6. Here we considered both the lossy case Fig. 5.6(a)-(c) and the lossless case (dashed curves in Fig. 5.6(d)-(f). The lossless results are obtained by solving the same coupled mode equation 5.17 by setting the imaginary part of the propagation constants (for the isolated and coupled modes) to 0. For the lossless case, the optical power in the optical waveguides will transfer to the pl waveguide and then transfer back without power dissipation during propagation. For the lossy case, the propagation loss in the pl waveguide is around 2102 dB/cm (calculated from the mode complex propagation constant), and the light coupled from optical to pl waveguide will be soon dissipated. As a result, there is no power transfer back and forth between two waveguides. The phase-matching condition plays an important role in affecting the coupling behavior. For the lossless case, as expected, the phase matching condition will effectively alter the maximum transfer power to the other waveguide. Almost 100% power transfer can be obtained under the perfect phase matching condition (Fig. 5.6(f)), and near 0% light can be transferred onto the other waveguide for a phase mismatch case (Fig. 5.6 (d)). For the lossy case, the phase matching condition will affect the optical power decay rate in both optical and pl waveguides. Phase matching will increase the optical propagation loss while phase mismatch will decrease the optical propagation loss. This provides us a possible way to reduce the metalinduced optical losses in optical waveguide by intentionally designing the modulator to make the optical and pl modes be phase mismatched. The detailed method has been discussed in [Paper \mathbb{C}].

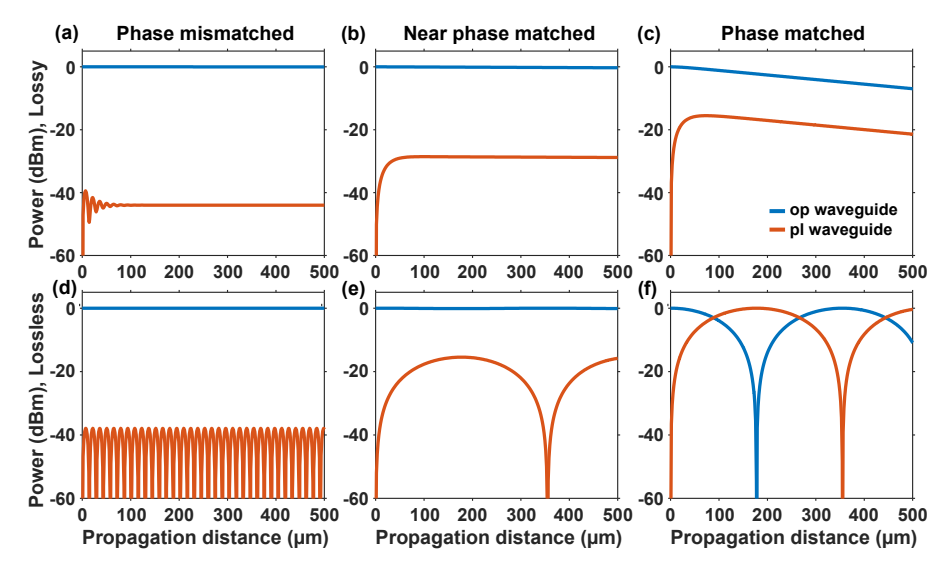


Figure 5.6: Calculated optical propagation properties in the two waveguide coupled system based on the CMT. The optical input is set to only from the optical waveguide. And the propagation constants used in the CMT calculations are from a finite element method (FEM) simulations based on the mode solver in COMSOL. (a)-(c) are the calculated results by considering a complex propagation constants - the lossy case, and the (d)-(f) are the lossless case by using a pure real propagation constant.

5.5 Traveling-wave modulator dynamic response

For most of the applications, we want to drive EO modulators at a high RF frequency, and dynamic responses need to be analyzed to obtain frequency-dependent modulation performance.

5.5.1 Mathematic description

For high-speed operation, traveling wave (TW) modulators are often adopted. The utilization of a traveling microwave enables a distributed modulator structure, significantly improving modulation performance. In this design, the RF signal is fed from the source through a coaxial connector onto a coplanar waveguide (CPW) transmission line (the electrode) and terminated at the end by an RF load. Optical and RF waves

undergo a synchronous interaction in the modulation region when their velocities are matched. With proper design, pure accumulation of optical phase can be achieved along the entire interaction length.

The RF waveguide is a quasi-TEM transmission line, whose voltage can be expressed:

$$V(z,t) = V^{+}e^{-(\beta_{m}z + \alpha_{m})z + i\omega_{m}t} + V^{-}e^{(\beta_{m}z + \alpha_{m})z + i\omega_{m}t},$$
 (5.19)

where the ω_m is the RF wave angular frequency, α_m is the RF attenuation constant, and $\beta_m=\frac{\omega_m}{v_m}=\frac{2\pi}{\lambda_m}$ is the RF propagation constant. Now we consider a photon with group velocity v_o coming in the mod-

ulator, the time the photon reaches position z is:

$$t = \frac{z}{v_o}. (5.20)$$

Define:

$$\beta_o = \frac{\omega_m}{v_o},\tag{5.21}$$

it should be noted here that the β_o is not an optical propagation constant. We can now rewrite equation 5.19 as:

$$V(z) = V^{+}e^{i(\beta_o - \beta_m)z - \alpha_m z} + V^{-}e^{i(\beta_o + \beta_m)z + \alpha_m z}, \qquad (5.22)$$

and the phase change due to EO modulation can be written as:

$$\Phi(\omega_m) = \frac{\pi}{V_{\pi}L} \int_{-L}^{0} V(z)dz$$

$$= \frac{\pi}{V_{\pi}L} (T_1 + T_2),$$
(5.23)

where the:

$$T_{1} = V^{+} \int_{-L}^{0} e^{i(\beta_{o} - \beta_{m})z - \alpha_{m}z} dz$$

$$= V^{+} \frac{1 - e^{-i(\beta_{o} - \beta_{m})L + \alpha_{m}L}}{i(\beta_{o} - \beta_{m}) - \alpha_{m}},$$

$$(5.24)$$

$$T_2 = V^{-} \int_{-L}^{0} e^{i(\beta_o + \beta_m)z + \alpha_m z} dz$$

$$= V^{-} \frac{1 - e^{-i(\beta_o + \beta_m)L - \alpha_m L}}{i(\beta_o + \beta_m) + \alpha_m}.$$
(5.25)

Here, T_1, T_2 represent the optical interaction with forward and backward RF waves, respectively. The forward and backward RF wave amplitude coefficients V^+ , V^- can be simply obtained from the TW EO modulator transmission line model, as shown in Fig. 5.7, considering the boundary conditions at the source (node 1) and load (node 2) [130]. Note that equation 5.23 can be used to model arbitrary electrodes of EO modulator as long as the electrodes can be treated as serials of connected transmission lines.

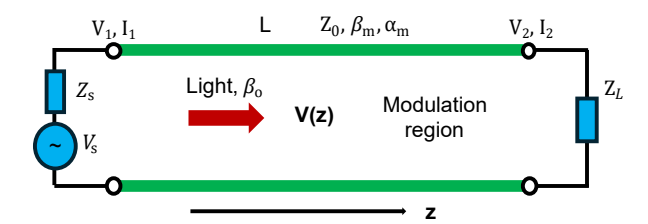


Figure 5.7: Transmission line model of the traveling-wave modulator.

By assuming impedance matching at all RF frequencies between the characteristic impedance Z_0 and the load impedance Z_L (no reflections in the transmission line), the modulation frequency response of the TW modulator can be expressed as [131,132]:

$$H(\omega_m) = \left| \frac{\Phi(\omega_m)}{\Phi(0)} \right|$$

$$= \frac{Z_{in}}{Z_{in} + Z_S} e^{-\alpha_m L/2} \sqrt{\frac{\sinh^2(\frac{\alpha_m L}{2}) + \sin^2(\frac{(\beta_o - \beta_m)L}{2})}{(\frac{\alpha_m L}{2})^2 + (\frac{(\beta_o - \beta_m)L}{2})^2}},$$
(5.26)

where Z_s and Z_{in} are the source impedance and the input impedance looking from the source and:

$$Z_{in} = Z_0 \frac{Z_L + Z_0 tanh(\beta_m L + \alpha_m L)}{Z_0 + Z_L tanh(\beta_m L + \alpha_m L)}$$

$$(5.27)$$

Equation 5.26 shows that the modulator frequency response is dominated by the following factors: (1) the RF loss of the transmission line; (2) the velocity mismatch between the optical and RF waves; (3) the impedance mismatch between line, source and load. Note that the impedance mismatch will lead to reflection and generate standing waves; and for TW modulators, the impedance is usually designed to be matched. By designing a modulator with strong impedance mismatch,

one can build an RF resonator and improve modulation efficiency with the sacrifice of EO bandwidth.

5.5.2 Influence of RF losses

RF loss can dissipate the drive signal and degrade the modulation performance. The existence of RF loss leads to a voltage amplitude decay for RF wave along the propagation direction, and the EO modulation will be weaker after longer distance propagation. Furthermore, the RF loss in the LN modulator is frequency dependent and the loss is approximately linearly proportional to the root of the RF frequency $(\alpha_m \propto \sqrt{f_m})$, which leads to a weaker EO modulation for higher frequency (a decrease in the EO BW), as shown in 5.8. The RF loss is inherit in a modulator which is dominated by the conductor ohmic losses from finite resistivity of metals. In principle, ohmic losses could be reduced by choosing electrode materials with higher electric conductivity. Today, most LN modulators use gold as electrodes because of its good conductivity $(4.52 \times 10^7 \text{ S/m})$ and chemical stability. Alternative options with better conductivity, such as silver $(6.30 \times 10^7 \text{ S/m})$ and copper $(5.98 \times 10^7 \text{ S/m})$, are hardly used and require further study to verify performance and reduce fabrication complexity.

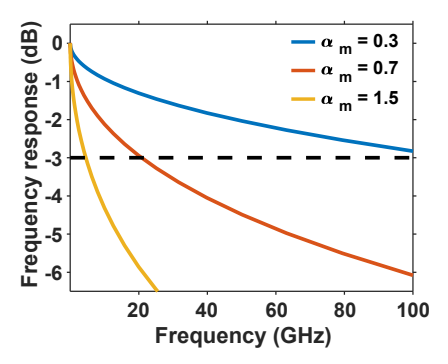


Figure 5.8: Calculated frequency response of a typical LN modulator, with different RF loss. Unit in the legend is $dB/cm/\sqrt{GHz}$. The electrode length is set to be 2 cm, the source and load impedance are matched to the transmission line, and the optical index and RF index are set to be equal (velocity matched).

5.5.3 Influence of velocity matching

Velocity matching is another important factor for the design of a high-speed EO modulator. Fig. 5.9 shows a similar calculation as in Fig. 5.8,

considering different velocity-matching conditions. The velocity matching we are talking about here is the matching between the group velocity of the optical wave and the phase velocity of the RF wave. For a monochromatic laser beam (CW light) entering the modulation region, the optical velocity in equation 5.20 should be interpreted as a phase velocity; however, as soon as phase modulation takes place, the optical signal becomes a narrow-band modulated signal, and the wavefront propagation velocity should be the group velocity. This has been experimentally verified in [133].

For simplicity, in Fig. 5.9, we use the $\delta n = n_o - n_m$ to represent the velocity mismatch factor, where n_o represents the optical mode group index and n_m represents the RF mode effective index. In the calculation, we set the RF loss at a standard value of $0.7 \, \mathrm{dB/cm/\sqrt{GHz}}$ and the active modulation region to 2 cm. As expected, a larger velocity mismatch will lead to a worse EO bandwidth. The RF dielectric permittivity of LN is around 28 which is much larger than its optical permittivity of around 4.5. For the LN modulator, the optical mode index n_o is dominated by the optical permittivity of the material (around 4.5). And the RF mode index n_m is dominated by the RF permittivity of LN (around 28) and SiO₂ (4.2). By simply designing the thickness of the SiO₂ cladding layer (tuning the RF mode distribution), we can achieve a perfect velocity-matching condition.

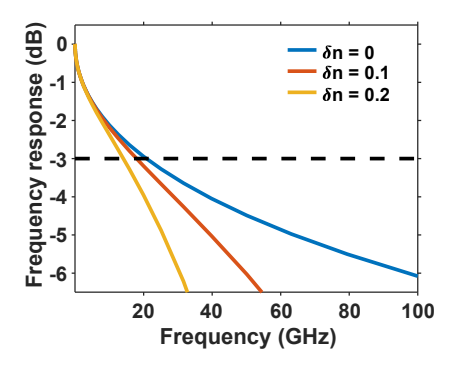


Figure 5.9: Calculated frequency response of a typical LN modulator, with different phase matching coefficient, $\delta n = n_o - n_m$. The electrode length is set to be 2 cm, the source and load impedance are matched to the transmission line, and the RF loss is set to be 0.7 dB/cm/ $\sqrt{\text{GHz}}$.

5.5.4 Influence of electrode length

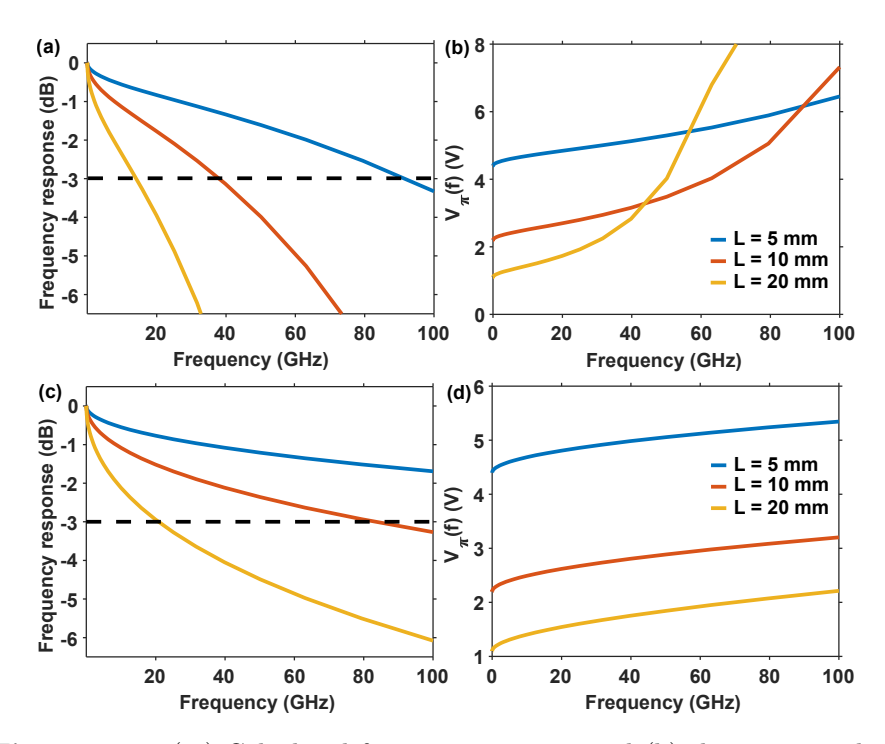


Figure 5.10: (a) Calculated frequency response and (b) the corresponding frequency dependent V_{π} of a typical LN modulator, with different electrodes length. In (a) and (b), the RF loss is set to be 0.7 dB/cm/ $\sqrt{\text{GHz}}$, the source and load impedance are matched to the transmission line, and the optical and RF velocities are set to be mismatched with $\delta n = 0.2$. In (c) and (d), all the conditions are set to be the same as in (a) and (b) except the velocity is set to be matched ($\delta n = 0$).

The influence of RF loss and velocity mismatch on EO BW is sensitive to the total electrode length. In Fig. 5.10 (a), we show another similar calculation result by considering different electrode lengths. The RF loss is set to $0.7~\mathrm{dB/cm/\sqrt{GHz}}$ and a velocity mismatching $\delta n = 0.2$ is used. The increase in electrode length will increase the total RF loss and the accumulated velocity mismatch. Based on the analysis of RF loss and velocity mismatch, we then get the conclusion that the EO bandwidth will decrease with increasing electrode length, as shown in Fig. 5.10 (a). It seems that we can simply reduce the electrode length to obtain a larger EO BW. However, this does not work since $V_{\pi}(DC)$ will increase significantly with the decrease of the electrode length, which is known as

the famous V_{π} -BW trade-off in the TW modulator. The trade-off only indicates the balance between BW and the $V_{\pi}(DC)$. For $V_{\pi}(f_m)$, the case becomes much more complicated. As shown in Fig. 5.10 (b), for low frequency range, the case is the same as in DC, V_{π} will be smaller with increasing electrode length; however, for extremely high frequency cases, the longer electrodes will give a much larger V_{π} . Due to the velocity mismatch, for long enough electrodes at high RF frequency, the waveguide phase change may change its sign over the modulation region and cancel with each other, thus may lead to an inverse trend for V_{π} over electrode length. By turning off the velocity mismatch, as shown in Fig. 5.10(c), (d), the $V_{\pi}(f)$ become normal and are always smaller for longer electrodes. The high frequency $V_{\pi}(f_m)$ is calculated by equation [116]:

$$V_{\pi}(f_m) = V_{\pi}(DC)10^{-\frac{H(f_m)}{20}}$$
 (5.28)

5.6 Segmented electrodes

As we discussed in the last section, for the high-speed integrated LN modulator, the main performance limiting factor is the high RF loss. A typical RF loss in the LN modulator is around $0.7~\mathrm{dB/cm/\sqrt{GHz}}$, which will limit the achievable EO bandwidth to a few tens of gigahertz (for example, for an electrode length of 2 cm).

For an LN modulator, the gap between the electrodes g should be minimized to obtain a smaller $V_{\pi}L$. However, RF loss is highly dependent on the distance from the signal to the ground pads g, and a small g tends to give a much higher RF loss due to the electrical current crowding effect. By introducing the so-called segmented electrodes, the current crowding effect can be largely suppressed and RF loss can be significantly reduced [134]. Fig. 5.11 shows the comparison between normal uniform electrodes and segmented electrodes (also called periodically loaded electrodes). The uniform electrode is a transmission line with a propagation constant γ and characteristic impedance Z, and

$$\gamma = \sqrt{(R + i\omega L)(G + i\omega C)}, Z = \sqrt{\frac{R + i\omega L}{G + i\omega C}},$$
 (5.29)

where the R, L, G, C represent the distributed resistance (with unit Ω/m), inductance (with unit H/m), capacitance (with unit F/m) and conductance (with unit S/m). The segmented electrode can be treated as a uniform electrode that is periodically loaded with a T-section (Fig.

5.11(b)). In the transmission line model, this is equivalent to a periodic circuit (Fig. 5.11(d)). Under the assumption that the loading period t is way smaller than the RF wavelength λ_m ($t \ll \lambda_m$), the loaded line is equivalent to a uniform transmission line with a new propagation constant γ_p and characteristic impedance Z_p :

$$\gamma_p = \sqrt{(R + i\omega L)(G + i\omega C + Y_a/t)}, Z_p = \sqrt{\frac{R + i\omega L}{G + i\omega C + Y_a/t}},$$
 (5.30)

Here Y_a is the admittance of the shunt load from the T sections, which is:

$$Y_a = \frac{1}{R + i\omega_m L + \frac{1}{i\omega_m C}}. (5.31)$$

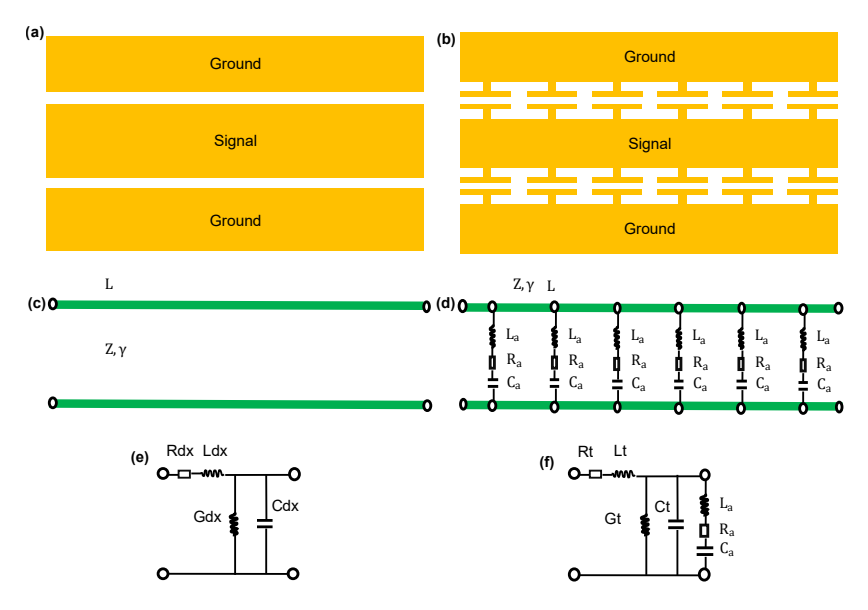


Figure 5.11: Layout of (a) uniform electrodes and (b) segmented electrodes; (c), (d) the corresponding transmission line models; and (e), (f) the corresponding equivalent circuit model for a short distance transmission line, t is the loading period.

Using such a segmented electrode, the RF loss could be significantly reduced while maintaining a similar low $V_{\pi}L$ compared to the uniform electrode. As a result, the EO BW can be increased to more than 100 GHz with a DC V_{π} of around 1 V, making it attractive for modern complex electro-optic links.

Chapter 6

Future outlook

This thesis presents a tightly confined LN waveguide platform with ultralow loss by carefully optimizing the nanofabrication process including exposure and etching. Our waveguide can achieve a few dB/m loss and extremely high light confinement with a bending radius as small as 20 μ m. Taking advantage of the developed waveguide platform, we demonstrated a few nonlinear applications: supercontinuum generation, Kerr soliton combs, and stimulated Brillouin scattering. We also focused on high-speed EO modulators in LN and proposed a design method to overcome the modulators' performance limit. Combined with micro-transfer printing, we demonstrated a heterogeneous integrated LN-Si₃N₄ EO modulator with a simulated large bandwidth. Despite the progress achieved in this thesis, further improvements and investigations are still needed.

- Towards lower waveguide loss Although we have achieved the state-of-the-art low-loss waveguide with a loss of a few dB/m, the waveguide loss is still far from the limit of loss of material absorption in LN (< 0.1 dB/m). Further optimization of the LN fabrication method is desired to obtain waveguides with smoother sidewalls. Introducing post-processes like mechanical or ion beam polishing may be another possible way for smoother sidewalls. A post-thermal process such as annealing for the LN waveguide may help to release the defects introduced during the smart-cut process in LNOI fabrication.
- Efficient EO modulators EO modulators in LN is a promising topic. Further study can be continued based on the work in this thesis. An experimental demonstration for the design in [Paper C]

will help us to understand the loss mechanism in LN EO modulators and achieve more efficient EO modulators. Moreover, introducing an RF resonator into EO modulators may significantly increase the modulation efficiency and reduce modulator footprints.

• Combining EO, χ^2 , χ^3 , and SBS on a single chip LN is a highly versatile photonic platform that enables various photonic devices. However, given time and resource constraints, our research is currently limited to single discrete photonic devices. In the future, the combination of devices using different material properties in LN and the building of a more complex on-chip photonic system will be promising.

Chapter 7

Summary of papers

Paper A

Compact lithium niobate microring resonators in the ultrahigh q/v regime, Opt. Lett. 48, 3949, 2023.

In this work, ultra-high Q/V (1 order of magnitude increasing compared with other results) optical resonators were demonstrated. With such high Q and low mode volume, we demonstrated ultra-high repetition rate and large bandwidth soliton microcombs.

My contributions: I developed the nanofabrication recipe to achieve high-Q optical mirroring resonators. I designed and fabricated all optical devices in lithium niobate. I performed linear and microcomb measurements. I analyzed the data and wrote the paper with the help of coauthors.

Paper B

Tightly-Confined and Long Z-Cut Lithium Niobate Waveguide with Ultralow-Loss, Laser Photonics Rev, p. e00042, 2025.

In this work, an ultralow-loss lithium niobate long waveguide was demonstrated with loss down to 5.8 dB/m for the first time. With such a low-loss long waveguide, we demonstrated an octave spanning supercontinuum frequency comb in the normal dispersion regime in LN waveguide for the first time.

My contributions: I polished the nanofabrication recipe developed in [Paper A], to achieve ultralow-loss long LN waveguides. I designed and fabricated the optical device. I performed the linear and supercontinuum measurements. I analyzed the data and wrote the paper with the help of coauthors.

Paper C

Suppressed plasmonic mode coupling for efficient electro-optic lithium niobate modulator, Manuscript accepted by Opt. Express, 2025.

In this work, we analyzed the optical absorption loss in a standard lithium niobate modulator and found that the loss is dominated by the mode coupling between the optical waveguide mode and the plasmonic modes. We proposed a new electrode design to reduce such metal-induced absorption loss by suppressing the mode coupling. We numerically demonstrated that such a design could reduce the loss by a factor of 5 and improve the modulation efficiency by around 15%.

My contributions: I conceived the idea with the help of my supervisors. I developed the simulation program and performed the device design and optimization. I wrote the paper with the help of coauthors.

Paper D

Fabrication Tolerant Heterogeneously Integrated Lithium Niobate Modulator on Bi-Layer Silicon Nitride Using Micro Transfer Printing, in Conference on Lasers and Electro-Optics Europe (CLEO/Europe), CE-6.2, 2025.

In this paper, we demonstrated an LN-SiN modulator with simulated $V_{\pi}L = 3.6$ Vcm and a 3-dB bandwidth of over 100 GHz. The LN layer was microtransfer printed onto a SiN wafer. The device could utilize the advantages of high Pockels effect in LN and ultralow loss in SiN.

My contributions: I developed the first simulation model for the modulator and assisted in the modulator design.

Paper E

Suspended Z-cut lithium niobate waveguides for stimulated Brillouin scattering, submitted, under review in APL Photonics, preprint available: arXiv:2504.07333, 2025.

In this paper, we demonstrated on-chip stimulated Brillouin scattering (SBS) in a suspended thin-film lithium niobate waveguide. This work demonstrated the first SBS (other works are based on surface SBS) in TFLN. We showed successful trapping of multiple 8.5 GHz – 9.5 GHz phonons in our structure, featuring a multi-peak Brillouin gain spectrum.

My contributions: I fabricated the device. I assisted in the waveguide design and paper writing.

References

- [1] P. Marin-Palomo, J. N. Kemal, M. Karpov, A. Kordts, J. Pfeifle, M. H. Pfeiffer, P. Trocha, S. Wolf, V. Brasch, M. H. Anderson et al., "Microresonator-based solitons for massively parallel coherent optical communications," *Nature*, vol. 546, no. 7657, pp. 274–279, 2017.
- [2] B. Corcoran, M. Tan, X. Xu, A. Boes, J. Wu, T. G. Nguyen, S. T. Chu, B. E. Little, R. Morandotti, A. Mitchell et al., "Ultra-dense optical data transmission over standard fibre with a single chip source," Nat. Commun., vol. 11, no. 1, p. 2568, 2020.
- [3] T. W. Hänsch, "Nobel lecture: passion for precision," *Rev. Mod. Phys.*, vol. 78, no. 4, pp. 1297–1309, 2006.
- [4] J. L. Hall, "Nobel lecture: Defining and measuring optical frequencies," *Rev. Mod. Phys.*, vol. 78, no. 4, pp. 1279–1295, 2006.
- [5] S. Wehner, D. Elkouss, and R. Hanson, "Quantum internet: A vision for the road ahead," *Science*, vol. 362, no. 6412, p. eaam9288, 2018.
- [6] T. D. Ladd, F. Jelezko, R. Laflamme, Y. Nakamura, C. Monroe, and J. L. O'Brien, "Quantum computers," *Nature*, vol. 464, no. 7285, pp. 45–53, 2010.
- [7] J. G. Fujimoto, "Optical coherence tomography for ultrahigh resolution in vivo imaging," *Nat. Biotechnol.*, vol. 21, no. 11, pp. 1361–1367, 2003.
- [8] R. Prevedel, A. Diz-Muñoz, G. Ruocco, and G. Antonacci, "Brillouin microscopy: an emerging tool for mechanobiology," Nat. Methods., vol. 16, no. 10, pp. 969–977, 2019.

- [9] S. E. Miller, "Integrated optics: An introduction," Bell Syst. Tech. J., vol. 48, no. 7, pp. 2059–2069, 1969.
- [10] C. R. Doerr, "Silicon photonic integration in telecommunications," Front. Phys., vol. 3, p. 37, 2015.
- [11] G. T. Reed, G. Mashanovich, F. Y. Gardes, and D. Thomson, "Silicon optical modulators," *Nat. Photonics*, vol. 4, no. 8, pp. 518–526, 2010.
- [12] G. Murdoch, A. Milenin, C. Delvaux, P. Ong, S. Pathak, D. Vermeulen, G. Sterckx, G. Winroth, P. Verheyen, G. Lepage et al., "Advanced 300-mm waferscale patterning for silicon photonics devices with record low loss and phase errors," in 17th Opto-Electronics and Communications Conference (OECC-2012). IEEE, 2012, pp. 15–16.
- [13] W. Jin, Q.-F. Yang, L. Chang, B. Shen, H. Wang, M. A. Leal, L. Wu, M. Gao, A. Feshali, M. Paniccia et al., "Hertz-linewidth semiconductor lasers using cmos-ready ultra-high-q mi-croresonators," Nat. Photonics, vol. 15, no. 5, pp. 346–353, 2021.
- [14] B. Shen, L. Chang, J. Liu, H. Wang, Q.-F. Yang, C. Xiang, R. N. Wang, J. He, T. Liu, W. Xie et al., "Integrated turnkey soliton microcombs," *Nature*, vol. 582, no. 7812, pp. 365–369, 2020.
- [15] M. Jahed, A. Caut, J. Goyvaerts, M. Rensing, M. Karlsson, A. Larsson, G. Roelkens, R. Baets, and P. O'Brien, "Angled flipchip integration of vesels on silicon photonic integrated circuits," *J. Light. Technol.*, vol. 40, no. 15, pp. 5190–5200, 2022.
- [16] L. Chang, M. H. Pfeiffer, N. Volet, M. Zervas, J. D. Peters, C. L. Manganelli, E. J. Stanton, Y. Li, T. J. Kippenberg, and J. E. Bowers, "Heterogeneous integration of lithium niobate and silicon nitride waveguides for wafer-scale photonic integrated circuits on silicon," Opt. Lett., vol. 42, no. 4, pp. 803–806, 2017.
- [17] T. Vanackere, T. Vandekerckhove, L. Bogaert, M. Billet, S. Poelman, S. Cuyvers, J. Van Kerrebrouck, A. Moerman, O. Caytan, N. Singh et al., "Heterogeneous integration of a high-speed lithium niobate modulator on silicon nitride using micro-transfer printing," APL Photonics, vol. 8, no. 8, 2023.

- [18] C. Xiang, J. Liu, J. Guo, L. Chang, R. N. Wang, W. Weng, J. Peters, W. Xie, Z. Zhang, J. Riemensberger et al., "Laser soliton microcombs heterogeneously integrated on silicon," Science, vol. 373, no. 6550, pp. 99–103, 2021.
- [19] W.-Q. Wei, A. He, B. Yang, Z.-H. Wang, J.-Z. Huang, D. Han, M. Ming, X. Guo, Y. Su, J.-J. Zhang et al., "Monolithic integration of embedded iii-v lasers on soi," *Light sci. appl.*, vol. 12, no. 1, p. 84, 2023.
- [20] M. Smit, K. Williams, and J. Van Der Tol, "Past, present, and future of inp-based photonic integration," *APL Photonics*, vol. 4, no. 5, 2019.
- [21] Y. Xuan, Y. Liu, L. T. Varghese, A. J. Metcalf, X. Xue, P.-H. Wang, K. Han, J. A. Jaramillo-Villegas, A. Al Noman, C. Wang et al., "High-q silicon nitride microresonators exhibiting low-power frequency comb initiation," Optica, vol. 3, no. 11, pp. 1171–1180, 2016.
- [22] X. Ji, F. A. Barbosa, S. P. Roberts, A. Dutt, J. Cardenas, Y. Okawachi, A. Bryant, A. L. Gaeta, and M. Lipson, "Ultra-lowloss on-chip resonators with sub-milliwatt parametric oscillation threshold," *Optica*, vol. 4, no. 6, pp. 619–624, 2017.
- [23] J. Liu, A. S. Raja, M. Karpov, B. Ghadiani, M. H. Pfeiffer, B. Du, N. J. Engelsen, H. Guo, M. Zervas, and T. J. Kippenberg, "Ultralow-power chip-based soliton microcombs for photonic integration," Optica, vol. 5, no. 10, pp. 1347–1353, 2018.
- [24] Z. Ye, K. Twayana, P. A. Andrekson, and V. Torres-Company, "High-q si3n4 microresonators based on a subtractive processing for kerr nonlinear optics," *Opt. Express*, vol. 27, no. 24, pp. 35719– 35727, 2019.
- [25] M. Pu, L. Ottaviano, E. Semenova, and K. Yvind, "Efficient frequency comb generation in algaas-on-insulator," *Optica*, vol. 3, no. 8, pp. 823–826, 2016.
- [26] L. Chang, W. Xie, H. Shu, Q.-F. Yang, B. Shen, A. Boes, J. D. Peters, W. Jin, C. Xiang, S. Liu et al., "Ultra-efficient frequency comb generation in algaas-on-insulator microresonators," Nat. Commun., vol. 11, no. 1, p. 1331, 2020.

- [27] H. Jung, K. Y. Fong, C. Xiong, and H. X. Tang, "Electrical tuning and switching of an optical frequency comb generated in aluminum nitride microring resonators," *Opt. Lett.*, vol. 39, no. 1, pp. 84–87, 2013.
- [28] M. A. Guidry, K. Y. Yang, D. M. Lukin, A. Markosyan, J. Yang, M. M. Fejer, and J. Vučković, "Optical parametric oscillation in silicon carbide nanophotonics," *Optica*, vol. 7, no. 9, pp. 1139– 1142, 2020.
- [29] M. Zhang, C. Wang, R. Cheng, A. Shams-Ansari, and M. Lončar, "Monolithic ultra-high-q lithium niobate microring resonator," *Optica*, vol. 4, no. 12, pp. 1536–1537, 2017.
- [30] Y. He, Q.-F. Yang, J. Ling, R. Luo, H. Liang, M. Li, B. Shen, H. Wang, K. Vahala, and Q. Lin, "Self-starting bi-chromatic linbo 3 soliton microcomb," *Optica*, vol. 6, no. 9, pp. 1138–1144, 2019.
- [31] Z. Gong, X. Liu, Y. Xu, M. Xu, J. B. Surya, J. Lu, A. Bruch, C. Zou, and H. X. Tang, "Soliton microcomb generation at 2 μ m in z-cut lithium niobate microring resonators," *Opt. Lett.*, vol. 44, no. 12, pp. 3182–3185, 2019.
- [32] Y. Gao, F. Lei, M. Girardi, Z. Ye, R. Van Laer, V. Torres-Company, and J. Schröder, "Compact lithium niobate microring resonators in the ultrahigh q/v regime," Opt. Lett., vol. 48, no. 15, pp. 3949– 3952, 2023.
- [33] Y. Gao, Y. Sun, I. Rebolledo-Salgado, R. Van Laer, V. Torres-Company, and J. Schröder, "Tightly-confined and long z-cut lithium niobate waveguide with ultralow-loss," *Laser Photonics Rev*, p. e00042, 2025.
- [34] D. Zhu, L. Shao, M. Yu, R. Cheng, B. Desiatov, C. Xin, Y. Hu, J. Holzgrafe, S. Ghosh, A. Shams-Ansari et al., "Integrated photonics on thin-film lithium niobate," Adv. Opt. Photonics, vol. 13, no. 2, pp. 242–352, 2021.
- [35] A. Boes, L. Chang, C. Langrock, M. Yu, M. Zhang, Q. Lin, M. Lončar, M. Fejer, J. Bowers, and A. Mitchell, "Lithium niobate photonics: Unlocking the electromagnetic spectrum," *Science*, vol. 379, no. 6627, p. eabj4396, 2023.

- [36] C. Wang, Z. Li, J. Riemensberger, G. Lihachev, M. Churaev, W. Kao, X. Ji, J. Zhang, T. Blesin, A. Davydova et al., "Lithium tantalate photonic integrated circuits for volume manufacturing," Nature, vol. 629, no. 8013, pp. 784–790, 2024.
- [37] Y. Qi and Y. Li, "Integrated lithium niobate photonics," *Nanophotonics*, vol. 9, no. 6, pp. 1287–1320, 2020.
- [38] A. Honardoost, K. Abdelsalam, and S. Fathpour, "Rejuvenating a versatile photonic material: thin-film lithium niobate," *Laser Photonics Rev.*, vol. 14, no. 9, p. 2000088, 2020.
- [39] R. Weis and T. Gaylord, "Lithium niobate: Summary of physical properties and crystal structure," *Appl. Phys. A.*, vol. 37, no. 4, pp. 191–203, 1985.
- [40] K. Nassau, H. Levinstein, and G. Loiacono, "Ferroelectric lithium niobate. 1. growth, domain structure, dislocations and etching," J. Phys. Chem. Solids., vol. 27, no. 6-7, pp. 983–988, 1966.
- [41] K. Nassau, H. Levinstein, and G. Loiacono, "Ferroelectric lithium niobate. 2. preparation of single domain crystals," *J. Phys. Chem. Solids.*, vol. 27, no. 6-7, pp. 989–996, 1966.
- [42] G. Peterson, A. Ballman, P. Lenzo, and P. Bridenbaugh, "Electrooptic properties of linbo3," *Appl. Phys. Lett.*, vol. 5, no. 3, pp. 62–64, 1964.
- [43] R. Smith, K. Nassau, and M. Galvin, "Efficient continuous optical second-harmonic generation," *Appl. Phys. Lett.*, vol. 7, no. 10, pp. 256–258, 1965.
- [44] R. Schmidt and I. Kaminow, "Metal-diffused optical waveguides in linbo3," *Appl. Phys. Lett.*, vol. 25, no. 8, pp. 458–458, 1974.
- [45] J. L. Jackel, C. Rice, and J. Veselka, "Proton exchange for high-index waveguides in linbo3," *Appl. Phys. Lett.*, vol. 41, no. 7, pp. 607–608, 1982.
- [46] G. Poberaj, H. Hu, W. Sohler, and P. Guenter, "Lithium niobate on insulator (lnoi) for micro-photonic devices," *Laser Photonics Rev.*, vol. 6, no. 4, pp. 488–503, 2012.

- [47] L. Chang, Y. Li, N. Volet, L. Wang, J. Peters, and J. E. Bowers, "Thin film wavelength converters for photonic integrated circuits," *Optica*, vol. 3, no. 5, pp. 531–535, 2016.
- [48] A. Rao, A. Patil, P. Rabiei, A. Honardoost, R. DeSalvo, A. Paolella, and S. Fathpour, "High-performance and linear thinfilm lithium niobate mach-zehnder modulators on silicon up to 50 ghz," Opt. Lett., vol. 41, no. 24, pp. 5700-5703, 2016.
- [49] L. Chen, Q. Xu, M. G. Wood, and R. M. Reano, "Hybrid silicon and lithium niobate electro-optical ring modulator," *Optica*, vol. 1, no. 2, pp. 112–118, 2014.
- [50] M. Churaev, R. N. Wang, A. Riedhauser, V. Snigirev, T. Blésin, C. Möhl, M. H. Anderson, A. Siddharth, Y. Popoff, U. Drechsler et al., "A heterogeneously integrated lithium niobate-on-silicon nitride photonic platform," Nat. Commun., vol. 14, no. 1, p. 3499, 2023.
- [51] R. Wu, M. Wang, J. Xu, J. Qi, W. Chu, Z. Fang, J. Zhang, J. Zhou, L. Qiao, Z. Chai et al., "Long low-loss-litium niobate on insulator waveguides with sub-nanometer surface roughness," *Nanomateri*als, vol. 8, no. 11, p. 910, 2018.
- [52] H. Hu, R. Ricken, W. Sohler, and R. Wehrspohn, "Lithium nio-bate ridge waveguides fabricated by wet etching," *IEEE Photonics Technol. Lett.*, vol. 19, no. 6, pp. 417–419, 2007.
- [53] G. Ulliac, V. Calero, A. Ndao, F. Baida, and M.-P. Bernal, "Argon plasma inductively coupled plasma reactive ion etching study for smooth sidewall thin film lithium niobate waveguide application," Opt. Mater., vol. 53, pp. 1–5, 2016.
- [54] H. Hu, A. Milenin, R. Wehrspohn, H. Hermann, and W. Sohler, "Plasma etching of proton-exchanged lithium niobate," J. Vac. Sci. Technol. A., vol. 24, no. 4, pp. 1012–1015, 2006.
- [55] H. Nagata, N. Mitsugi, K. Shima, M. Tamai, and E. Haga, "Growth of crystalline lif on cf4 plasma etched linbo3 substrates," J. Cryst. Growth, vol. 187, no. 3-4, pp. 573–576, 1998.
- [56] P. G. Glöersen, "Ion- beam etching," J. Vac. Sci. Technol., vol. 12, no. 1, pp. 28–35, 1975.

- [57] F. Chen, "Photonic guiding structures in lithium niobate crystals produced by energetic ion beams," *J. Appl. Phys.*, vol. 106, no. 8, 2009.
- [58] Z. Gong, X. Liu, Y. Xu, and H. X. Tang, "Near-octave lithium niobate soliton microcomb," *Optica*, vol. 7, no. 10, pp. 1275–1278, 2020.
- [59] B. Nie, X. Lv, C. Yang, R. Ma, K. Zhu, Z. Wang, Y. Liu, Z. Xie, X. Jin, G. Zhang et al., "Soliton microcombs in x-cut linbo3 microresonators," arXiv preprint arXiv:2502.07180, 2025.
- [60] Z. Li, R. N. Wang, G. Lihachev, J. Zhang, Z. Tan, M. Churaev, N. Kuznetsov, A. Siddharth, M. J. Bereyhi, J. Riemensberger et al., "High density lithium niobate photonic integrated circuits," Nat. Commun., vol. 14, no. 1, p. 4856, 2023.
- [61] C. Wang, M. Zhang, X. Chen, M. Bertrand, A. Shams-Ansari, S. Chandrasekhar, P. Winzer, and M. Lončar, "Integrated lithium niobate electro-optic modulators operating at cmos-compatible voltages," *Nature*, vol. 562, no. 7725, pp. 101–104, 2018.
- [62] M. He, M. Xu, Y. Ren, J. Jian, Z. Ruan, Y. Xu, S. Gao, S. Sun, X. Wen, L. Zhou et al., "High-performance hybrid silicon and lithium niobate mach-zehnder modulators for 100 gbit s- 1 and beyond," Nat. Photonics, vol. 13, no. 5, pp. 359–364, 2019.
- [63] J. Lu, J. B. Surya, X. Liu, A. W. Bruch, Z. Gong, Y. Xu, and H. X. Tang, "Periodically poled thin-film lithium niobate microring resonators with a second-harmonic generation efficiency of 250,000%/W," Optica, vol. 6, no. 12, pp. 1455–1460, 2019.
- [64] J.-Y. Chen, Z.-H. Ma, Y. M. Sua, Z. Li, C. Tang, and Y.-P. Huang, "Ultra-efficient frequency conversion in quasi-phase-matched lithium niobate microrings," *Optica*, vol. 6, no. 9, pp. 1244–1245, 2019.
- [65] L. Qu, W. Wu, W. Cai, M. Ren, and J. Xu, "Second harmonic generation in lithium niobate on insulator," *Laser Photonics Rev.*, p. 2401928, 2025.
- [66] C. Xin, S. Lu, J. Yang, A. Shams-Ansari, B. Desiatov, L. S. Magalhães, S. S. Ghosh, E. McGee, D. Renaud, N. Achuthan

- et al., "Wavelength-accurate and wafer-scale process for nonlinear frequency mixers in thin-film lithium niobate," Commun. Phys., vol. 8, no. 1, p. 136, 2025.
- [67] E. L. Wooten, K. M. Kissa, A. Yi-Yan, E. J. Murphy, D. A. Lafaw, P. F. Hallemeier, D. Maack, D. V. Attanasio, D. J. Fritz, G. J. McBrien et al., "A review of lithium niobate modulators for fiber-optic communications systems," J. Sel. Top. Quantum Electron., vol. 6, no. 1, pp. 69–82, 2000.
- [68] P. J. Bock, P. Cheben, J. H. Schmid, J. Lapointe, A. Delâge, S. Janz, G. C. Aers, D.-X. Xu, A. Densmore, and T. J. Hall, "Subwavelength grating periodic structures in silicon-on-insulator: a new type of microphotonic waveguide," *Opt. Express*, vol. 18, no. 19, pp. 20251–20262, 2010.
- [69] A. W. Snyder, J. D. Love et al., Optical waveguide theory. Chapman and hall London, 1983, vol. 175.
- [70] V. S. Ilchenko, A. A. Savchenkov, A. B. Matsko, and L. Maleki, "Nonlinear optics and crystalline whispering gallery mode cavities," *Phys. Rev. Lett.*, vol. 92, no. 4, p. 043903, 2004.
- [71] M. Leidinger, S. Fieberg, N. Waasem, F. Kühnemann, K. Buse, and I. Breunig, "Comparative study on three highly sensitive absorption measurement techniques characterizing lithium niobate over its entire transparent spectral range," Opt. Express, vol. 23, no. 17, pp. 21690–21705, 2015.
- [72] A. Shams-Ansari, G. Huang, L. He, Z. Li, J. Holzgrafe, M. Jankowski, M. Churaev, P. Kharel, R. Cheng, D. Zhu et al., "Reduced material loss in thin-film lithium niobate waveguides," APL Photonics, vol. 7, no. 8, 2022.
- [73] P. Rabiei, W. H. Steier, C. Zhang, and L. R. Dalton, "Polymer micro-ring filters and modulators," *J. Lightwave Technol.*, vol. 20, no. 11, p. 1968, 2002.
- [74] E. D. Moore, "Advances in swept-wavelength interferometry for precision measurements," Ph.D. dissertation, University of Colorado at Boulder, 2011.

- [75] P. Del'Haye, O. Arcizet, M. L. Gorodetsky, R. Holzwarth, and T. J. Kippenberg, "Frequency comb assisted diode laser spectroscopy for measurement of microcavity dispersion," *Nat. Photonics*, vol. 3, no. 9, pp. 529–533, 2009.
- [76] B. J. Soller, D. K. Gifford, M. S. Wolfe, and M. E. Froggatt, "High resolution optical frequency domain reflectometry for characterization of components and assemblies," *Opt. Express*, vol. 13, no. 2, pp. 666–674, 2005.
- [77] A. Maity, S. Maithani, and M. Pradhan, "Cavity ring-down spectroscopy: recent technological advancements, techniques, and applications," *Anal. Chem.*, vol. 93, no. 1, pp. 388–416, 2020.
- [78] G. Berden, R. Peeters, and G. Meijer, "Cavity ring-down spectroscopy: Experimental schemes and applications," *Int. Rev. Phys. Chem.*, vol. 19, no. 4, pp. 565–607, 2000.
- [79] D. Dai and M. Zhang, "Mode hybridization and conversion in silicon-on-insulator nanowires with angled sidewalls," *Opt. Express*, vol. 23, no. 25, pp. 32452–32464, 2015.
- [80] D. Dai, Y. Tang, and J. E. Bowers, "Mode conversion in tapered submicron silicon ridge optical waveguides," *Opt. Express*, vol. 20, no. 12, pp. 13425–13439, 2012.
- [81] A. A. Tseng, K. Chen, C. D. Chen, and K. J. Ma, "Electron beam lithography in nanoscale fabrication: recent development," *IEEE Trans. Compon. Packag. Manuf. Technol.*, vol. 26, no. 2, pp. 141–149, 2003.
- [82] R. Pease, "Electron beam lithography," Contemp. Phys., vol. 22, no. 3, pp. 265–290, 1981.
- [83] R. J. Bojko, J. Li, L. He, T. Baehr-Jones, M. Hochberg, and Y. Aida, "Electron beam lithography writing strategies for low loss, high confinement silicon optical waveguides," *J. Vac. Sci. Technol. B.*, vol. 29, no. 6, 2011.
- [84] M. Yu, Y. Okawachi, R. Cheng, C. Wang, M. Zhang, A. L. Gaeta, and M. Lončar, "Raman lasing and soliton mode-locking in lithium niobate microresonators," *Light Sci. Appl.*, vol. 9, no. 1, p. 9, 2020.

- [85] C. Wang, M. Zhang, M. Yu, R. Zhu, H. Hu, and M. Loncar, "Monolithic lithium niobate photonic circuits for kerr frequency comb generation and modulation," *Nat. Commun.*, vol. 10, no. 1, p. 978, 2019.
- [86] Y. He, H. Liang, R. Luo, M. Li, and Q. Lin, "Dispersion engineered high quality lithium niobate microring resonators," *Opt. Express*, vol. 26, no. 13, pp. 16315–16322, 2018.
- [87] J. Lu, J. B. Surya, X. Liu, Y. Xu, and H. X. Tang, "Octave-spanning supercontinuum generation in nanoscale lithium niobate waveguides," Opt. Lett., vol. 44, no. 6, pp. 1492–1495, 2019.
- [88] M. Yu, B. Desiatov, Y. Okawachi, A. L. Gaeta, and M. Lončar, "Coherent two-octave-spanning supercontinuum generation in lithium-niobate waveguides," Opt. Lett., vol. 44, no. 5, pp. 1222–1225, 2019.
- [89] R. Alfano and S. Shapiro, "Emission in the region 4000 to 7000 å via four-photon coupling in glass," Phys. Rev. Lett., vol. 24, no. 11, p. 584, 1970.
- [90] J. M. Dudley, G. Genty, and S. Coen, "Supercontinuum generation in photonic crystal fiber," Rev. Mod. Phys., vol. 78, no. 4, pp. 1135–1184, 2006.
- [91] N. Singh, D. Vermulen, A. Ruocco, N. Li, E. Ippen, F. X. Kärtner, and M. R. Watts, "Supercontinuum generation in varying dispersion and birefringent silicon waveguide," *Opt. Express*, vol. 27, no. 22, pp. 31698–31712, 2019.
- [92] A. R. Johnson, A. S. Mayer, A. Klenner, K. Luke, E. S. Lamb, M. R. Lamont, C. Joshi, Y. Okawachi, F. W. Wise, M. Lipson et al., "Octave-spanning coherent supercontinuum generation in a silicon nitride waveguide," Opt. Lett., vol. 40, no. 21, pp. 5117– 5120, 2015.
- [93] H. Hu, F. Da Ros, M. Pu, F. Ye, K. Ingerslev, E. Porto da Silva, M. Nooruzzaman, Y. Amma, Y. Sasaki, T. Mizuno et al., "Single-source chip-based frequency comb enabling extreme parallel data transmission," Nat. Photonics, vol. 12, no. 8, pp. 469–473, 2018.
- [94] H. Jung, C. Xiong, K. Y. Fong, X. Zhang, and H. X. Tang, "Optical frequency comb generation from aluminum nitride microring resonator," Opt. Lett., vol. 38, no. 15, pp. 2810–2813, 2013.

- [95] C.-S. Brès, A. Della Torre, D. Grassani, V. Brasch, C. Grillet, and C. Monat, "Supercontinuum in integrated photonics: generation, applications, challenges, and perspectives," *Nanophotonics*, vol. 12, no. 7, pp. 1199–1244, 2023.
- [96] Y. Okawachi, M. Yu, B. Desiatov, B. Y. Kim, T. Hansson, M. Lončar, and A. L. Gaeta, "Chip-based self-referencing using integrated lithium niobate waveguides," *Optica*, vol. 7, no. 6, pp. 702–707, 2020.
- [97] E. Obrzud, S. Denis, H. Sattari, G. Choong, S. Kundermann, O. Dubochet, M. Despont, S. Lecomte, A. H. Ghadimi, and V. Brasch, "Stable and compact rf-to-optical link using lithium niobate on insulator waveguides," *Apl Photonics*, vol. 6, no. 12, 2021.
- [98] M. Reig Escalé, F. Kaufmann, H. Jiang, D. Pohl, and R. Grange, "Generation of 280 thz-spanning near-ultraviolet light in lithium niobate-on-insulator waveguides with sub-100 pj pulses," *APL Photonics*, vol. 5, no. 12, 2020.
- [99] T.-H. Wu, L. Ledezma, C. Fredrick, P. Sekhar, R. Sekine, Q. Guo, R. M. Briggs, A. Marandi, and S. A. Diddams, "Visible-toultraviolet frequency comb generation in lithium niobate nanophotonic waveguides," *Nat. Photonics*, vol. 18, no. 3, pp. 218–223, 2024.
- [100] S. Lauria and M. F. Saleh, "Mixing second-and third-order non-linear interactions in nanophotonic lithium-niobate waveguides," Phys. Rev. A., vol. 105, no. 4, p. 043511, 2022.
- [101] G. P. Agrawal, "Nonlinear fiber optics," in *Nonlinear Science at the Dawn of the 21st Century*. Springer, 2000, pp. 195–211.
- [102] L. Yin, Q. Lin, and G. P. Agrawal, "Soliton fission and supercontinuum generation in silicon waveguides," Opt. Lett., vol. 32, no. 4, pp. 391–393, 2007.
- [103] J. M. Dudley and S. Coen, "Coherence properties of supercontinuum spectra generated in photonic crystal and tapered optical fibers," Opt. Lett., vol. 27, no. 13, pp. 1180–1182, 2002.

- [104] J. E. Rothenberg, "Femtosecond optical shocks and wave breaking in fiber propagation," Opt. Soc. Am. B., vol. 6, no. 12, pp. 2392– 2401, 1989.
- [105] M. Klimczak, G. Soboń, R. Kasztelanic, K. M. Abramski, and R. Buczyński, "Direct comparison of shot-to-shot noise performance of all normal dispersion and anomalous dispersion supercontinuum pumped with sub-picosecond pulse fiber-based laser," Sci. Rep., vol. 6, no. 1, p. 19284, 2016.
- [106] T. J. Kippenberg, R. Holzwarth, and S. A. Diddams, "Microresonator-based optical frequency combs," *Science*, vol. 332, no. 6029, pp. 555–559, 2011.
- [107] A. A. Savchenkov, A. B. Matsko, D. Strekalov, M. Mohageg, . f. V. S. Ilchenko, and L. Maleki, "Low threshold optical oscillations in a whispering gallery mode c a f 2 resonator," *Phys. Rev. Lett.*, vol. 93, no. 24, p. 243905, 2004.
- [108] T. Kippenberg, S. Spillane, and K. Vahala, "Kerr-nonlinearity optical parametric oscillation in an ultrahigh-q toroid microcavity," Phys. Rev. Lett., vol. 93, no. 8, p. 083904, 2004.
- [109] T. Herr, V. Brasch, J. D. Jost, C. Y. Wang, N. M. Kondratiev, M. L. Gorodetsky, and T. J. Kippenberg, "Temporal solitons in optical microresonators," *Nat. Photonics*, vol. 8, no. 2, pp. 145– 152, 2014.
- [110] T. Herr, M. L. Gorodetsky, and T. J. Kippenberg, "Dissipative kerr solitons in optical microresonators," Nonlinear optical cavity dynamics: from microresonators to fiber lasers, pp. 129–162, 2016.
- [111] J. Liu, G. Huang, R. N. Wang, J. He, A. S. Raja, T. Liu, N. J. Engelsen, and T. J. Kippenberg, "High-yield, wafer-scale fabrication of ultralow-loss, dispersion-engineered silicon nitride photonic circuits," *Nat. Commun.*, vol. 12, no. 1, p. 2236, 2021.
- [112] M.-G. Suh and K. Vahala, "Gigahertz-repetition-rate soliton microcombs," *Optica*, vol. 5, no. 1, pp. 65–66, 2018.
- [113] X. Liu, Z. Gong, A. W. Bruch, J. B. Surya, J. Lu, and H. X. Tang, "Aluminum nitride nanophotonics for beyond-octave soliton microcomb generation and self-referencing," *Nat. Commun.*, vol. 12, no. 1, p. 5428, 2021.

- [114] Y. Song, X. Zhu, X. Zuo, G. Huang, and M. Lončar, "Stable gigahertz-and mmwave-repetition-rate soliton microcombs on x-cut lithium niobate," *Optica*, vol. 12, no. 5, pp. 693–701, 2025.
- [115] J. Witzens, "High-speed silicon photonics modulators," *Proc. IEEE.*, vol. 106, no. 12, pp. 2158–2182, 2018.
- [116] M. Howerton, R. Moeller, A. Greenblatt, and R. Krahenbuhl, "Fully packaged, broad-band linbo 3 modulator with low drive voltage," *IEEE Photonics Technol. Lett.*, vol. 12, no. 7, pp. 792–794, 2000.
- [117] H. Feng, T. Ge, X. Guo, B. Wang, Y. Zhang, Z. Chen, S. Zhu, K. Zhang, W. Sun, C. Huang et al., "Integrated lithium niobate microwave photonic processing engine," *Nature*, vol. 627, no. 8002, pp. 80–87, 2024.
- [118] J. Lu, A. Al Sayem, Z. Gong, J. B. Surya, C.-L. Zou, and H. X. Tang, "Ultralow-threshold thin-film lithium niobate optical parametric oscillator," *Optica*, vol. 8, no. 4, pp. 539–544, 2021.
- [119] G. Chen, Y. Gao, H.-L. Lin, and A. J. Danner, "Compact and efficient thin-film lithium niobate modulators," Advanced Photonics Research, vol. 4, no. 12, p. 2300229, 2023.
- [120] M. Zhang, C. Wang, P. Kharel, D. Zhu, and M. Lončar, "Integrated lithium niobate electro-optic modulators: when performance meets scalability," *Optica*, vol. 8, no. 5, pp. 652–667, 2021.
- [121] G. Ghione et al., Semiconductor devices for high-speed optoelectronics. Cambridge University Press Cambridge, 2009, vol. 116.
- [122] https://www.comsol.com.
- [123] X. Guo, Y. Ma, Y. Wang, and L. Tong, "Nanowire plasmonic waveguides, circuits and devices," *Laser Photonics Rev.*, vol. 7, no. 6, pp. 855–881, 2013.
- [124] A. Tuniz, A. Y. Song, G. Della Valle, and C. M. de Sterke, "Coupled mode theory for plasmonic couplers," Appl. Phys. Rev., vol. 11, no. 2, 2024.
- [125] H. F. Taylor and A. Yariv, "Guided wave optics," Proc IEEE., vol. 62, no. 8, pp. 1044–1060, 1974.

- [126] M. Alam, J. S. Aitchison, and M. Mojahedi, "Theoretical analysis of hybrid plasmonic waveguide," *IEEE J. Sel. Top. Quantum Electron.*, vol. 19, no. 3, pp. 4602008–4602008, 2013.
- [127] R. F. Oulton, V. J. Sorger, D. Genov, D. Pile, and X. Zhang, "A hybrid plasmonic waveguide for subwavelength confinement and long-range propagation," *Nat. Photonics*, vol. 2, no. 8, pp. 496– 500, 2008.
- [128] A. Tuniz, M. A. Schmidt, and B. T. Kuhlmey, "Influence of non-hermitian mode topology on refractive index sensing with plasmonic waveguides," *Photonics Res.*, vol. 10, no. 3, pp. 719–730, 2022.
- [129] W.-P. Huang, "Coupled-mode theory for optical waveguides: an overview," J. Opt. Soc. Am. A, vol. 11, no. 3, pp. 963–983, 1994.
- [130] D. M. Pozar, Microwave engineering: theory and techniques. John wiley & sons, 2021.
- [131] H. Chung, W. S. Chang, and E. L. Adler, "Modeling and optimization of traveling-wave linbo/sub 3/interferometric modulators," *IEEE J. Quantum Electron.*, vol. 27, no. 3, pp. 608–617, 2002.
- [132] A. Honardoost, R. Safian, A. Rao, and S. Fathpour, "High-speed modeling of ultracompact electrooptic modulators," *J. Light. Tech*nol., vol. 36, no. 24, pp. 5893–5902, 2018.
- [133] R. Spickermann, S. R. Sakamoto, and N. Dagli, "In traveling wave modulators which velocity to match?" in *Conference Proceedings LEOS'96 9th Annual Meeting IEEE Lasers and Electro-Optics So*ciety, vol. 2. IEEE, 1996, pp. 97–98.
- [134] P. Kharel, C. Reimer, K. Luke, L. He, and M. Zhang, "Breaking voltage-bandwidth limits in integrated lithium niobate modulators using micro-structured electrodes," *Optica*, vol. 8, no. 3, pp. 357–363, 2021.

Papers

Paper A

Compact lithium niobate microring resonators in the ultrahigh \mathbf{q}/\mathbf{v} regime

Y. Gao, F. Lei, M. Girardi, Z. Ye, R. Van Laer, V. Torres-Company, and J. Schröder

Opt. Lett. 48, 3949, 2023.

Paper B

Tightly-Confined and Long Z-Cut Lithium Niobate Waveguide with Ultralow-Loss

Y. Gao, Y. Sun, I. Rebolledo-Salgado, R. Van Laer, V. Torres-Company, and J. Schröder

Laser Photonics Rev, p. e00042, 2025.

Paper C

Suppressed plasmonic mode coupling for efficient electro-optic lithium niobate modulator

Y. Gao, V. Torres-Company, and J. Schröder

Manuscript accepted by Opt. Express, 2025.

Paper D

Fabrication Tolerant Heterogeneously Integrated Lithium Niobate Modulator on Bi-Layer Silicon Nitride Using Micro Transfer Printing

V. Talebi, M. Girardi, Y. Gao, F. N. A. Labbé, V. Torres-Company, Y. Ding, M. Pu, and K. Yvind

In Conference on Lasers and Electro-Optics Europe (CLEO/Europe), CE-6.2, 2025.

Paper E

Suspended Z-cut lithium niobate waveguides for stimulated Brillouin scattering

L. Haerteis, Y. Gao, A. Dubey, M. K. Schmidt, P. Thurgood, G. Ren, J. Schröder, D. Marpaung, A. Mitchell, M. J. Steel, A. Boes

Submitted, under review in APL Photonics, preprint avaible: $arXiv:2504.07333,\ 2025.$